

Correspondence Distillation from NeRF-based GAN

Yushi Lan · Chen Change Loy · Bo Dai

Received: date / Accepted: date

Abstract The neural radiance field (NeRF) has shown promising results in preserving the fine details of objects and scenes. However, unlike mesh-based representations, it remains an open problem to build dense correspondences across different NeRFs of the same category, which is essential in many downstream tasks. The main difficulties of this problem lie in the implicit nature of NeRF and the lack of ground-truth correspondence annotations. In this paper, we show it is possible to bypass these challenges by leveraging the rich semantics and structural priors encapsulated in a pre-trained NeRF-based GAN. Specifically, we exploit such priors from three aspects, namely 1) a dual deformation field that takes latent codes as global structural indicators, 2) a learning objective that regards generator features as geometric-aware local descriptors, and 3) a source of infinite object-specific NeRF samples. Our experiments demonstrate that such priors lead to 3D dense correspondence that is accurate, smooth, and robust. We also show that established dense correspondence across NeRFs can effectively enable many NeRF-based downstream applications such as texture transfer.

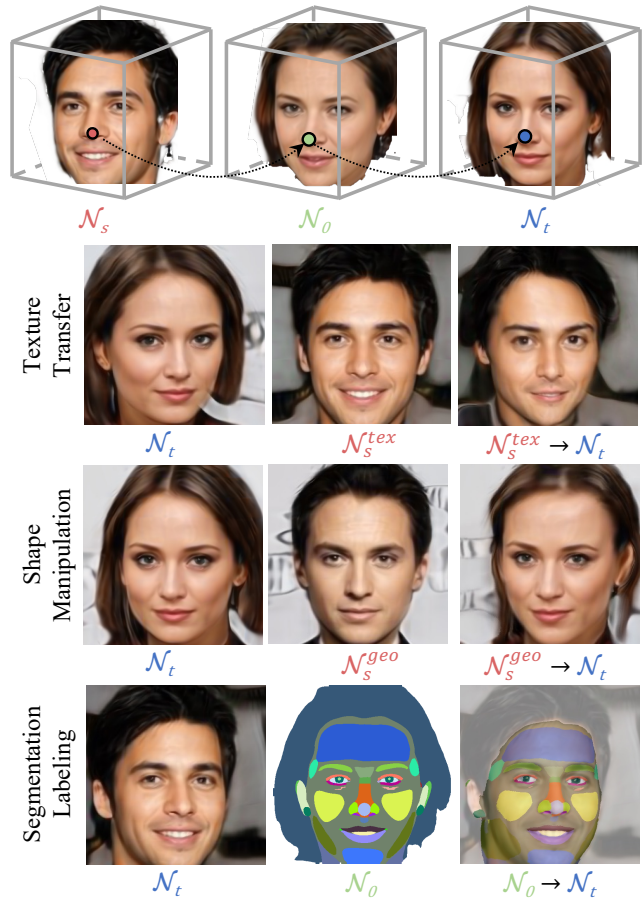


Fig. 1 Dense correspondence across two objects represented as NeRF. We propose Dual Deformation Field (DDF) to establish 3D dense correspondences between two objects represented as NeRF. This is achieved by a composite deformation (row 1): given a source-target NeRF pair \mathcal{N}_s and \mathcal{N}_t , which we aim to establish correspondences on, for a point \mathbf{x}_s from the source NeRF \mathcal{N}_s , we first establish its correspondence with a point on the template NeRF \mathcal{N}_o , which is further deformed to the target NeRF \mathcal{N}_t . Our training is fully self-supervised and could facilitate a series of downstream applications, such as texture transfer (row 2), shape manipulation (row 3) and 1-shot view-consistent segmentation transfer (row 4).

Yushi Lan
S-Lab, Nanyang Technological University, Singapore
E-mail: yushi001@e.ntu.edu.sg

Chen Change Loy
S-Lab, Nanyang Technological University, Singapore
E-mail: cclloy@ntu.edu.sg

Bo Dai
Shanghai AI Laboratory
E-mail: doubledaibo@gmail.com

1 Introduction

The success of neural radiance fields (NeRF) (Mildenhall et al., 2020) has led to remarkable progress in learning 3D representations. Unlike voxel- and mesh-based methods, NeRF represents each 3D object as a distribution of coordinate-based volume densities and view-dependent colors. And by approximating this distribution with a continuous parametric function, NeRF shows great potential in capturing geometric scene details and rendering realistic novel views.

In this work, we study the potential of *establishing dense correspondence across two objects represented as NeRF*, which is an important prerequisite for many downstream applications such as texture transfer, manipulation and segmentation transfer, as shown in the Fig. 1. This task is non-trivial. First, existing methods for building dense correspondence across two objects mainly focus on mesh-based representations. It is infeasible to directly apply and adapt them to NeRF. Unlike meshes that have explicit vertices and surfaces, NeRF lacks an explicit surface, preventing us from resorting derivatives of neural fields (Yang et al., 2021) as the shape surface descriptors. Moreover, existing methods (Litany et al., 2017) often require ground-truth correspondence annotations in training, which are hard to obtain for NeRF-based object representations.

To overcome the aforementioned limitations, we present a novel approach that exploits NeRF-based generative adversarial networks (GANs) (Chan et al., 2021a; Niemeyer and Geiger, 2021; Schwarz et al., 2020) to facilitate the learning of dense correspondence in NeRF. Specifically, NeRF-based GANs treat image synthesis as novel views rendering from its intermediate NeRF representation. Our key idea is to employ its generator, G , to play a **triple role**, as shown in Fig. 2:

1) Since the generator of a GAN is a latent variable model that learns a mapping $z \rightarrow G(z)$, the associated latent code z shall capture the underlying structure of the generated object NeRF $G(z)$ in a pretrained GAN. Therefore, this latent code naturally serves as a holistic global structure descriptor for building conditional models that generalize to different object NeRFs of a category of interest.

2) As a representation learning architecture, G can serve as a robust semantic embedding function that maps corresponding coordinates across different NeRFs into semantically similar features. Based on such cross-instance feature similarity, we can thus naturally use features by G as geometric-aware local descriptors.

3) G can also serve as a source of infinite object-specific NeRFs $\mathcal{N}_{i=1}^{\text{inf}}$ for training, where it is flexible to adjust

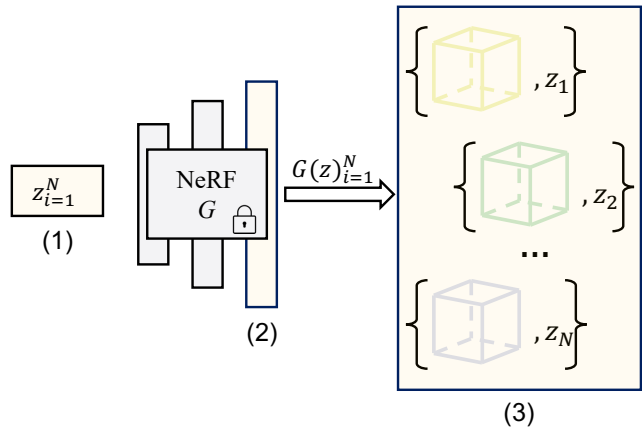


Fig. 2 The triple role of a NeRF-based GAN: We retrofit a pretrained NeRF-based GAN into triple roles: (1) the latent codes $z_{i=1}^N$ serve as holistic structure descriptors; (2) the extracted generator features serve as geometry-aware local descriptors; and (3) the sampling space of pretrained G could serve as an infinite object-specific dataset.

the complexity of sampled NeRFs through the latent codes.

We name our approach as **Dual Deformation Field (DDF)**. While our *DDF* does not limit the choice of NeRF-based GAN, we use π -GAN (Chan et al., 2021a) due to its simplicity and promising synthesis results. Our adaptation of the pre-trained π -GAN starts with considering its first role in model construction, where we treat latent codes of π -GAN as additional conditions. Specifically, we regard dense correspondence between NeRFs as a coordinate-based deformation field from the source NeRF to the target NeRF. Instead of learning a single deformation field conditioned on a pair of source and target latent codes, we use a fixed template NeRF as the bridge and learn two separate deformation fields, namely a backward deformation field B and a forward deformation field F . In our formulation, B always treats the template NeRF as the target, taking only the source latent code as input. Similarly, F always treats the template NeRF as the source, taking the target latent code as the condition. Such a decomposition substantially alleviates the learning complexity. In addition, the dense correspondence between any two NeRFs can be easily established by combining F and B .

Benefit from the second role of π -GAN, *DDF* can learn without ground-truth correspondence annotations. Specifically, for any coordinate in the source NeRF, we can obtain its corresponding coordinate in the target NeRF from *DDF*. Since the features of π -GAN are geometric-aware descriptors, we, therefore, compute generator features for these estimated cor-

responding coordinates and apply feature-wise cosine similarity as the primary learning objective.

Finally, as π -GAN provides infinite object-specific NeRF samples for training, in practice we further control the complexity of sampled NeRFs by mixing the latent codes of sampled NeRFs with that of the template NeRF, we can use training samples of low deformation complexity in the beginning, and gradually move to samples with higher complexity as training proceeds. We found this strategy improves the training-time efficiency and stability.

This is an early attempt that establishes the dense correspondence between two NeRF-based object representations. Without any ground-truth correspondence annotations, dense correspondence is established by mining rich semantic and structural priors from a pre-trained NeRF-based GAN. In the challenging category of human faces, the proposed method produces high-quality dense correspondences with promising robustness and generality. Various tasks such as texture transfer and segmentation transfer are tested to demonstrate the potential of our method in downstream tasks. Code and models will be released.

2 Related Work

3D Shape Correspondences. The problem of establishing dense correspondences between 3D shapes is of key importance to a series of downstream tasks (Egger et al., 2020; Loper et al., 2015), and has been studied extensively in recent survey (Kaick et al., 2011; Sahillioglu, 2019). Traditional approaches build correspondence between shapes represented by mesh or point clouds. They can be roughly divided into registration-based and similarity-based methods, where the former adopts Laplacian coordinate δ_i for vertex v_i as geometric preservation descriptor after registration. Similarity-based solutions do not change the geometry of given shapes and calculate the similarity between vertices with learnable feature descriptors. With recent advances in geometric machine learning (Qi et al., 2017; Wang et al., 2019b), researchers extend traditional framework by replacing hand-crafted descriptor with learnable feature descriptors (Fan et al., 2019; Litany et al., 2017; Zhou et al., 2016). Eisenberger et al. (2021); Halimi et al. (2019) further mitigate the requirements of correspondences annotations which builds soft correspondence matrix $\Pi \in \mathbb{R}^{m \times n}$ between numerable vertices on the mesh surface. The lack of explicit surface and numerable vertices in NeRF hinders the use of above methods, where correspondence affinity matrix (Eisenberger et al., 2021) could not be built. Pioneer works (Deng et al., 2021; Liu and Liu, 2020;

Zheng et al., 2021) propose to build correspondences over implicit representations. However, they still rely on ground-truth reconstruction annotations to train the deformation field. Collecting such annotations for NeRF-based representations is infeasible, where there are infinite points with non-zero densities.

Neural Implicit Representations for 3D Geometry. The success of deep learning over 2D domain has spurred a growing interest in the 3D domain. However, traditional explicit representation such as mesh and voxel are hard to fit in deep learning optimization framework due to the varying topology or limited resolution. As a parallel class of shape representation, recent advances in implicit functions (Chen and Zhang, 2019; Mescheder et al., 2019; Park et al., 2019) have demonstrated their excellence when representing complicated geometry. By representing shapes as a continuous field, implicit representation encodes the geometry properties of a 3D point x using a neural network $f(x)$. Conventional implicit representations were limited by the need of 3D ground-truth. NeRF (Mildenhall et al., 2020) stands out as a successful variant to support direct learning of 3D scene from multi-view images. Guo et al. (2021); Li et al. (2021); Park et al. (2021a,c); Pumarola et al. (2020) further improve NeRF to model non-rigid and time-varying scenes by equipping static NeRF MLP with an extra deformation field. Gafni et al. (2021); Hong et al. (2022); Noguchi et al. (2021); Wang et al. (2021); Zheng et al. (2022) augment NeRF MLP with a template shape using 3D basic models, including 3DMM (Gafni et al., 2021; Hong et al., 2022), FLAME (Zheng et al., 2022) and SMPL (Noguchi et al., 2021) to enable more explicit control. However, they are still limited to overfitting setting and the learned models fail to generalize to novel scenes. Please note that implicit shape representation and neural rendering are still developing rapidly and we refer readers to the survey (Tewari et al., 2020) for more details.

Though great advances have been achieved, building dense correspondence across shapes represented by implicit functions are intrinsically challenging since ground truth correspondence are impossible to acquire. Recent attempts to build correspondence over implicit representations (Deng et al., 2021; Zheng et al., 2021) tried to bypass this requirement by defining F as signed distance function (SDF) values of the deformed points and d as the marginal L_1 loss as in (Park et al., 2019). Liu and Liu (2020) followed similar principles as functional maps and adopted occupancy loss as supervision, while the basis functions are learned from data. Though dense correspondence over implicit functions could be derived, these methods are unable to establish consistent bijective correspondence and still require 3D super-

vision during training. Moreover, these methods are all constrained on synthetic dataset (Chang et al., 2015), which limit the applications on real scenes.

Our method is different from them in three ways. First, our method builds on NeRF that has been shown more effective in representing realistic scenes. Second, our method is fully free of 3D annotations like sparse correspondence labeling or 3D models. This uniqueness of our method facilitates more downstream applications where only 2D images are available. Lastly, our method builds bijective correspondences between two NeRFs, offering more flexibility and scalability to deform between two NeRFs.

Generative Models and 3D-aware Image Synthesis. Deep generative models, especially GANs (Brock et al., 2019; Goodfellow et al., 2014; Karras et al., 2019a), have shown promising results in generating photorealistic images. To further extend GANs to synthesize images in a 3D-consistent manner, many recent approaches investigated how to incorporate 3D inductive bias into generative training. Motivated by the success of NeRF (Mildenhall et al., 2020), pioneer work (Chan et al., 2021a; Schwarz et al., 2020) resorted to the continuous power of radiance fields as the incorporated 3D inductive bias in GANs, which have paved the way for this field. Impressive results have been achieved on both 3D-aware image synthesis and multi-view consistency. More 3D-aware GANs (Chan et al., 2021b; Gu et al., 2022; Niemeyer and Geiger, 2021; Or-El et al., 2021; Zhou et al., 2021) are proposed to support faster rendering (Niemeyer and Geiger, 2021), better shape modeling (Chan et al., 2021b; Or-El et al., 2021), as well 3D style transfer (Zhou et al., 2021). Without loss of generality, here we employ the basic π -GAN (Chan et al., 2021a) architecture as both a robust correspondence similarity metric and an infinite source of 3D NeRFs. Beyond the study of improving the synthesis quality, few work probes how to apply the representations learned by GANs for downstream tasks. Some studies (Bau et al., 2020; Shen et al., 2020) interpret the semantics encoded by GANs and apply them for image editing. Other works (Tritrong et al., 2021; Zhang et al., 2021a,b) leverage the rich semantics in GAN’s features for fine-grained annotation synthesis, few-shot segmentation as well as multi-view data generation, respectively. Concurrently Eslami et al. (2018); Jahanian et al. (2020); Pan et al. (2021); Zhang et al. (2021a) show that GAN trained on 2D images can learn implicit notion of 3D environment. But it remains much less explored whether the learned GAN representations are transferable to more challenging 3D tasks, like dense correspondence estimation.

3 Methodology

In this paper, we present a new attempt for building dense correspondence between NeRF representations across objects belonging to the same category. Obtaining ground-truth correspondence annotations is infeasible due to the implicit nature of NeRF. Our key insight is to retrofit a generator of a pre-trained NeRF-based π -GAN, denoted as G , into triple roles: 1) the latent codes in G serve as holistic global structure indicators that improve the generality of models; 2) the features of G serve as geometric-aware local descriptors that enable a feature-based learning objective; 3) and the manifold of G serves as a source of infinite training and evaluation samples over a single category.

In the following sections, we first introduce the details of NeRF-based π -GAN in Sec. 3.1 as the background knowledge for subsequent sections. Next, we explain the problem formulation and our framework in Sec. 3.2, learning objective in Sec. 3.3, and training strategy in Sec. 3.4.

3.1 Background on NeRF-based GANs

Inspired by the success of NeRF as an efficient 3D representation, NeRF-based GANs employ NeRF as their internal representation for 3D-aware image synthesis. We adopt π -GAN (Chan et al., 2021a) in this paper. Specifically, the generator of the π -GAN contains a mapping network \mathcal{M} and a multi-layer perceptron (MLP) network. Starting from a latent code $\mathbf{z} \sim p_Z$ that follows the Gaussian prior distribution, the mapping network first maps \mathbf{z} to a set of modulation signals $\mathcal{M}(\mathbf{z}) = \{\boldsymbol{\beta}, \boldsymbol{\gamma}\}$, where $\boldsymbol{\beta} = \{\beta_i\}, \boldsymbol{\gamma} = \{\gamma_i\}$. In π -GAN, a NeRF is obtained by the MLP network, which estimates the view-dependent density $\sigma \in \mathbb{R}^+$ and the color vector $\mathbf{c} \in \mathbb{R}^3$ for each 3D point, taking its coordinate $\mathbf{x} \in \mathbb{R}^3$ and a viewing direction $\mathbf{d} \in \mathbb{S}^2$ as input. To associate a latent code to its corresponding NeRF, the modulation signals will be injected into the MLP network, serving as FiLM conditions (Dumoulin et al., 2018; Perez et al., 2018; Sitzmann et al., 2020) to modulate its features at different layers as $\mathbf{f}_{i+1} = \sin(\gamma_i \cdot (\mathbf{W}_i \mathbf{f}_i + \mathbf{b}_i) + \beta_i)$.

Image synthesis in π -GAN is achieved by sampling a latent code and subsequently rendering an image from the corresponding NeRF. Following the volume rendering of NeRF (Mildenhall et al., 2020), each pixel color C of the image is obtained via sampling a set of points along the ray $r(t) = \mathbf{o} + t\mathbf{d}$ and accumulating their color

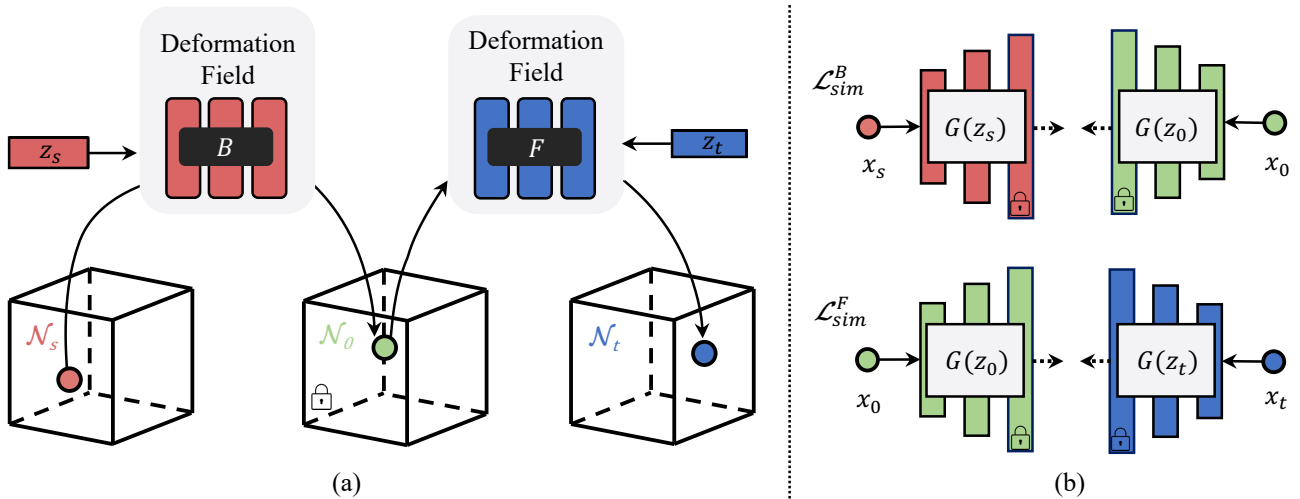


Fig. 3 Overview of the proposed Dual Deformation Field (DDF). (a) DDF consists of two coordinate-based deformation fields, namely the backward B and the forward F . To get the correspondence point given a point \mathbf{x}_s sampled from the source NeRF \mathcal{N}_s , the B model conditions on the \mathbf{z}_s and learns to deform the input point \mathbf{x}_s to the correspondence point in the template NeRF \mathcal{N}_0 . Similarly, the F model conditions on the target latent code \mathbf{z}_t and learns to deform points from the template NeRF \mathbf{x}_0 to the target NeRF \mathcal{N}_t . (b): Feature similarity losses \mathcal{L}_{sim}^B and \mathcal{L}_{sim}^F between features extracted from the generator of the pre-trained π -GAN, G , is adopted as the main loss. Please refer to Fig. 5 for the details of the other two supervisions imposed in the training.

vectors weighted by their transmittance:

$$\hat{C}(\mathbf{r}) = \sum_{i=1}^N T(t_i)(1 - \exp(-\sigma_i \delta_i)) \mathbf{c}_i, \quad (1)$$

where $T(t) = \exp\left(-\sum_{j=1}^{i-1} \sigma_j \delta_j\right)$ and $\delta_i = t_{i+1} - t_i$ is the distance between adjacent samples. Using a set of unposed 2D images, π -GAN is trained progressively with the non-saturating GAN loss and the R1 regularization (Mescheder et al., 2018).

3.2 The Proposed Framework

Problem Formulation. Given any pair of NeRFs $\mathcal{N}_s : \mathbb{R}^3 \mapsto \mathbb{R}^4$ and $\mathcal{N}_t : \mathbb{R}^3 \mapsto \mathbb{R}^4$, our goal is to estimate a 3D deformation residual $H_D : \mathbb{R}^3 \mapsto \mathbb{R}^3$ that deforms NeRF \mathcal{N}_s towards NeRF \mathcal{N}_t via:

$$\mathcal{N}_s \rightarrow \mathcal{N}_t : \mathbf{x}_t = (\mathbf{x}_s + H_D(\mathbf{x}_s)), \forall \mathbf{x}_s \in \mathcal{N}_s. \quad (2)$$

The deformation field H_D represents the residual 3D deformation $D(\mathbf{x}_s) = \Delta \mathbf{x}_s$ in the 3D space of the source NeRF \mathcal{N}_s . It is an injective mapping that maps each 3D point \mathbf{x}_s in the source NeRF, \mathcal{N}_s , to its corresponding position in the target NeRF, \mathcal{N}_t .

Challenges. The problem formulation shown above follows existing attempts (Deng et al., 2021; Zheng et al., 2021) that model the dense 3D correspondences between an SDF shape and a shared template via a single deformation field. However, this design does not suit

NeRF for the following reasons. First, their parameterization is designed to facilitate shape reconstruction, rather than establishing correspondences between two existing shapes. Second, deforming all the points on a shape to a shared template could only guarantee an injective mapping instead of a bijective mapping, where a random point over the template could not find its correspondence on a target shape. Third, this design limits information (e.g., textures) propagation between NeRFs. Given a ray that intersects with a shape, unlike SDF representation where the shape surface is modeled by a single point on the zero-level iso-surface, the volume-based representation (e.g., NeRF) represents the shape boundary by innumerable points (Zhang et al., 2020). Therefore, after the source NeRF, \mathcal{N}_s , deforms densely sampled near-surface points with texture information to the template, it is computationally intractable for the target NeRF, \mathcal{N}_t , to find the precise corresponding texture for points along a ray.

Dual Deformation Field. We propose to fix the above-mentioned issues by lifting the injective mapping to a bijective mapping function. A straightforward solution here is to leverage a single conditional mapping function $D : \mathbb{R}^3 \times \mathbb{R}^{\mathbf{z}_t} \times \mathbb{R}^{\mathbf{z}_s} \mapsto \mathbb{R}^3$, which estimates the offset for each point \mathbf{x} of the source NeRF \mathcal{N}_s , taking its coordinate and the latent codes \mathbf{z}_t and \mathbf{z}_s of target and source NeRFs as input. However, since the source and target NeRFs vary in each iteration, such a solution requires a large model capacity and fails to converge in practice. A similar observation has also

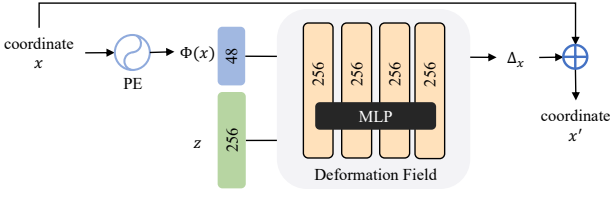


Fig. 4 A diagram of the deformation field model architecture. Both the forward deformation field F and the backward deformation field B are implemented as MLPs consisting of four fully-connected layers with residual connections (Mildenhall et al., 2020; Yu et al., 2021). Both F and B take a latent code \mathbf{z} of 256 dimensions and a coordinate as input, where the latter is embedded into a 48-dimensional vector via positional encoding (Mildenhall et al., 2020; Tancik et al., 2020)

been proposed in previous work that models dynamic NeRF (Pumarola et al., 2020).

To alleviate the computational complexity without sacrificing the bijective property, as illustrated in Fig. 3, we sample a fixed NeRF with a latent code \mathbf{z}_0 from G as the intermediate template \mathcal{N}_0 , and reformulate the deformation field D as the composition of two separate conditional neural deformation fields, namely, a backward deformation field B that estimates the deformation from a source NeRF, \mathcal{N}_s , to the template \mathcal{N}_0 , and a forward deformation field F that estimates the deformation from the template \mathcal{N}_0 to a target NeRF, \mathcal{N}_t .

By decomposing the deformation field between two arbitrary NeRFs into two fields B and F bridged by a fixed template NeRF, the overall learning complexity is significantly reduced. In this way we have

$$\mathbf{x}_0 = B(\mathbf{x}_s, \mathbf{z}_s), \quad B(\mathbf{x}_s, \mathbf{z}_s) := \mathbf{x}_s + H_B(\phi(\mathbf{x}_s), \mathbf{z}_s), \quad (3)$$

$$\mathbf{x}_t = F(\mathbf{x}_0, \mathbf{z}_t), \quad F(\mathbf{x}_0, \mathbf{z}_t) := \mathbf{x}_0 + H_F(\phi(\mathbf{x}_0), \mathbf{z}_t), \quad (4)$$

where $\mathbf{x}_s \in \mathcal{N}_s$, $\mathbf{x}_t \in \mathcal{N}_t$, and $\mathbf{x}_0 \in \mathcal{N}_0$. And $\phi(\mathbf{x})$ is the positional encoding (Mildenhall et al., 2020) of a given point. H_B and H_F are residual functions each implemented as an MLP consisting of four fully-connected layers, as depicted in Fig. 4. The correspondence point of $\mathbf{x}_s \in \mathcal{N}_s$ in a target NeRF \mathcal{N}_t can be retrieved by the composite mapping $F(B(\mathbf{x}_s, \mathbf{z}_s), \mathbf{z}_t)$, as depicted in Fig. 3. The latent codes \mathbf{z}_s and \mathbf{z}_t serve as the holistic global structure indicators to guide the deformation. Implementation wise, the template NeRF \mathcal{N}_0 is chosen as $(\bar{\gamma}, \bar{\beta})$ which can be intuitively seen as the average shape of the trained dataset.

3.3 Training Objective

Our overall training objective contains a feature similarity loss for estimated correspondences and three additional regularizations for the deformation fields F and B , namely a cycle-consistency regularization, a second-order feature similarity loss, and a deformation smoothness regularization.

Generator Feature Similarity Loss. Given a collection of n source NeRFs $\{\mathcal{N}_s^{(i)}\}_{i=1}^n$ that are sampled from G with corresponding latent codes $\{\mathbf{z}_s^{(i)}\}_{i=1}^n$, each of these NeRFs will serve as a source NeRF for B to compute its deformation to the template. For each pair of estimated corresponding points $(\mathbf{x}_s, \mathbf{x}_0)$ where \mathbf{x}_s belongs to one of these source NeRFs and \mathbf{x}_0 belongs to the template, we take a point feature extracted from NeRF generator G as the local geometric descriptor. When the \mathbf{x}_s and \mathbf{x}_0 are homologous and share similar semantic meanings, the feature similarity loss should be small, and a smaller feature similarity loss in training indicates that the deformation field produces reasonable correspondences. Therefore, for each pair of sampled points, we compare the cosine similarity between two descriptors as their correspondence relevance score and update the network accordingly. Consequently, the feature similarity loss for B can be written as:

$$\mathcal{L}_{sim}^B = \frac{1}{n} \sum_{i=1}^n \left[\frac{1}{|\mathcal{P}_s^{(i)}|} \sum_{\mathbf{x}_s \in \mathcal{P}_s^{(i)}} w_{\mathbf{x}_s} * \frac{1}{2} \|G(\mathbf{x}_s, \mathbf{z}_s^{(i)}) - G(B(\mathbf{x}_s, \mathbf{z}_s^{(i)}), \mathbf{z}_0)\|_2^2 \right], \quad (5)$$

where the loss of each point $\mathbf{x}_s^{(i)}$ is weighted by $w_{\mathbf{x}_s} = T(t_{\mathbf{x}_s})$ defined in Eq. 1, so that B is encouraged to focus more on points with large densities, as they are close to the object surface with rich semantics. It is worth noting that to reduce computational redundancy and complexity, we will sample only a subset $\mathcal{P}_s^{(i)}$ of points from each NeRF $\mathcal{N}_s^{(i)}$ by the sampling strategy introduced in the next section. Each of these NeRFs will also serve as a target NeRF for F to compute the deformation of the template to it. The feature similarity loss for F is thus:

$$\mathcal{L}_{sim}^F = \frac{1}{m} \sum_{j=1}^m \left[\frac{1}{|\mathcal{P}_0^{(j)}|} \sum_{\mathbf{x}_0 \in \mathcal{P}_0^{(j)}} w_{\mathbf{x}_0} * \frac{1}{2} \|G(\mathbf{x}_0, \mathbf{z}_0) - G(F(\mathbf{x}_0, \mathbf{z}_t^{(j)}), \mathbf{z}_t^{(j)})\|_2^2 \right], \quad (6)$$

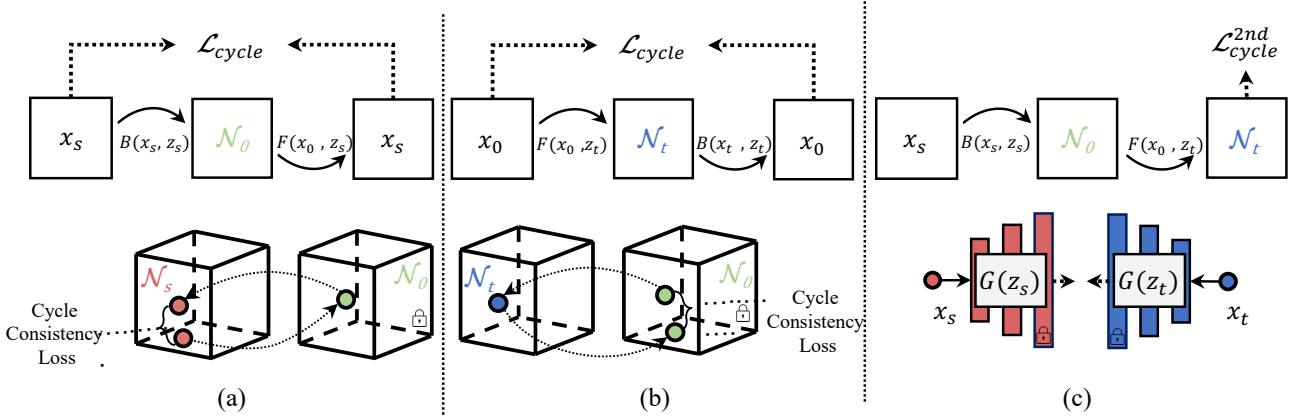


Fig. 5 Illustration of loss functions used in DDF. (a) Backward cycle-consistency loss: $F(B(\mathbf{x}_s, \mathbf{z}_s), \mathbf{z}_s) \approx \mathbf{x}_s$, (b) forward cycle-consistency loss: $B(F(\mathbf{x}_t, \mathbf{z}_t), \mathbf{z}_t) \approx \mathbf{x}_t$ and (c) second-order feature similarity loss: $G(\mathbf{x}_s, \mathbf{z}_s) \approx G(F(B(\mathbf{x}_s, \mathbf{z}_s), \mathbf{z}_t), \mathbf{z}_t)$.

where \mathbf{x}_0 stands for a point on the template \mathcal{N}_0 and we sample a subset $\mathcal{P}_0^{(j)}$ from \mathcal{N}_0 for each different target NeRF $\mathcal{N}_t^{(j)}$. For all the feature similarity supervision, we adopt features of G at multiple layers and concatenate them to better reflect the semantics of a point. We justify our choice in Sec. 4.5.

Cycle-Consistency Regularization. Since the conditional deformation fields, F and B , are supposed to restore the original deformation field D , when the same NeRF \mathcal{N}_i is used as both the source and target NeRF, they should satisfy $D(\mathbf{x}, \mathbf{z}_t, \mathbf{z}_t) = \mathbf{x}$ for all valid points \mathbf{x} . As depicted in Fig. 5(a,b), we further apply a cycle-consistency regularization for B and F :

$$\mathcal{L}_{cycle} = \frac{1}{n} \sum_{i=1}^n \left[\frac{1}{|\mathcal{P}_s^{(i)}|} \sum_{\mathbf{x}_s \in \mathcal{P}_s^{(i)}} \|F(B(\mathbf{x}_s, \mathbf{z}_s^{(i)}), \mathbf{z}_s^{(i)}) - \mathbf{x}_s\|_2^2 \right] + \frac{1}{m} \sum_{j=1}^m \left[\frac{1}{|\mathcal{P}_0^{(j)}|} \sum_{\mathbf{x}_0 \in \mathcal{P}_0^{(j)}} \|B(F(\mathbf{x}_0, \mathbf{z}_t^{(j)}), \mathbf{z}_t^{(j)}) - \mathbf{x}_0\|_2^2 \right]. \quad (7)$$

Second-Order Feature Similarity Loss. Apart from the aforementioned point-wise cycle-consistency loss that regularizes the deformation coherency of learned mapping, we also combine it with Eq. 5, 6 and impose a feature-based cross-instance cycle-consistency loss. Specifically, for a given point \mathbf{x}_s in a source NeRF $\mathcal{N}_s^{(i)}$ paired with latent code $\mathbf{z}_s^{(i)}$, beyond imposing the similarity regularization only over the template NeRF \mathcal{N}_0 , we further deform its intermediate point $\mathbf{x}_0 = B(\mathbf{x}_s, \mathbf{z}_s)$ to a randomly sampled paired target

NeRF $\mathcal{N}_t^{(i)}$ and calculate their feature similarity:

$$\mathcal{L}_{cycle}^{2nd} = \frac{1}{n} \sum_{i=1}^n \left[\frac{1}{|\mathcal{P}_s^{(i)}|} \sum_{\mathbf{x}_s \in \mathcal{P}_s^{(i)}} w_{\mathbf{x}_s} * \frac{1}{2} \|G(F(B(\mathbf{x}_s, \mathbf{z}_s^{(i)}), \mathbf{z}_t^{(i)}), \mathbf{z}_t^{(i)}), G(\mathbf{x}_s, \mathbf{z}_s^{(i)})\|_2^2 \right]. \quad (8)$$

We find this auxiliary regularization improves cross-instance deformation consistency.

Deformation Smoothness Regularization. To encourage the smoothness of deformation and reduce spatial distortion, a deformation smoothness regularization is also included. Here we penalize the norm of the Jacobian matrix $\mathbb{J}_D = \nabla D$ of the deformation fields (Park et al., 2021b) to ensure the learned deformations are physically smooth:

$$\mathcal{L}_{smooth} = \frac{1}{n} \sum_{i=1}^n \left[\frac{1}{|\mathcal{P}_s^{(i)}|} \sum_{\mathbf{x}_s \in \mathcal{P}_s^{(i)}} \max(\|\nabla B(\mathbf{x}_s, \mathbf{z}_s^{(i)})\|_2^2 - \epsilon, 0) \right] + \frac{1}{m} \sum_{j=1}^m \left[\frac{1}{|\mathcal{P}_0^{(j)}|} \sum_{\mathbf{x}_0 \in \mathcal{P}_0^{(j)}} \max(\|\nabla F(\mathbf{x}_0, \mathbf{z}_t^{(j)})\|_2^2 - \epsilon, 0) \right], \quad (9)$$

where ϵ is the slack parameter for the smoothness regularization. The final objective is thus $\mathcal{L}_{total} = \mathcal{L}_{sim}^F + \mathcal{L}_{sim}^B + \lambda_{cycle} \mathcal{L}_{cycle} + \lambda_{cycle}^{2nd} \mathcal{L}_{cycle}^{2nd} + \lambda_{smooth} \mathcal{L}_{smooth}$ where λ_{cycle} , λ_{cycle}^{2nd} , and λ_{smooth} are balancing coefficients, which are respectively set to 1, 0.1 and 10^{-4} in practice.

3.4 Training Strategy

While the pre-trained π -GAN G serves as a source of infinite object NeRFs, in each iteration of the training process we will sample a batch of source NeRFs $\{\mathcal{N}_s^{(i)}\}_{i=1}^n$ with corresponding latent codes $\{\mathbf{z}_s^{(i)}\}_{i=1}^n$, and a batch of target NeRFs $\{\mathcal{N}_t^{(j)}\}_{j=1}^m$ with the corresponding latent codes $\{\mathbf{z}_t^{(j)}\}_{j=1}^m$. To further sample a point set for each sampled NeRF $\mathcal{N}_*^{(i)}$, for each pixel within the resolution $H \times W$ we shoot a ray $r(v) = \mathbf{o} + v\mathbf{d}$ where \mathbf{d} identifies the direction from the camera to the pixel. Subsequently, for each ray we follow Mildenhall et al. (2020) and conduct a hierarchical sampling to obtain a *fine* set of points, *i.e.*, points near the object surface. We denote the union of these point sets sampled from source as $\{\mathcal{P}_s^{(i)}\}_{i=1}^n$, which are used to train the B model. Since the points sampled to train F models are all from the template NeRF \mathcal{N}_0 , here we denote the the point sets paired with target NeRF $\mathcal{N}_t^{(j)}$ as $\{\mathcal{P}_0^{(j)}\}_{j=1}^m$ for clarity.

Curriculum Sampling of NeRFs. In practice, we find the variation between the sampled NeRF and the template NeRF can significantly affect the training process, which may even collapse at the beginning stage if it gets a sampled NeRF that differs substantially from the template.

To improve training stability and efficiency, we adopt a curriculum sampling strategy to obtain NeRFs from G , by gradually morphing the template NeRF in the latent space to sample NeRFs with growing complexity. Specifically, since in π -GAN, the semantics of a sampled NeRF is determined by the modulation signals (β, γ) , we can linearly interpolate between two sets of modulation signals to gradually morph one NeRF into another. Inspired by this property of π -GAN, when we sample a set of n NeRFs $\{\mathcal{N}^{(i)}\}_{i=1}^n$, we compute their corresponding modulation signals $\{(\beta^{(i)}, \gamma^{(i)})\}_{i=1}^n$ from their latent codes. Subsequently, we adjust the learning complexity by blending them with the template NeRF as

$$\beta^{(i)}(\alpha) = \beta_0 + \alpha \cdot (\beta^{(i)} - \beta_0) \quad (10)$$

$$\gamma^{(i)}(\alpha) = \gamma_0 + \alpha \cdot (\gamma^{(i)} - \gamma_0), \quad (11)$$

where (β_0, γ_0) are the modulation signals of the template NeRF and α controls the learning difficulty. In practice, we start from $\alpha = 0$ and linearly increase the value to 0.6 during training, which is a reasonable value to balance sampling quality and diversity (Karras et al., 2019b). In this way, the model learns to produce identity deformation first and then gradually evolves to model more complicated deformation when trained on more challenging samples.

4 Experiments

4.1 Experimental Setup

As discussed in (Deng et al., 2021; Zheng et al., 2021), there is no ground-truth dense correspondence dataset available for structure with variations. Therefore, we adopt three proxy tasks as surrogate metrics to evaluate the learned correspondences of DDF . In Sec. 4.2, we first qualitatively demonstrate the dense correspondences learned by DDF through texture transfer. Quantitative results are shown in two alternative tasks, namely fine-grained segmentation transfer and keypoints transfer, in Sec. 4.3 and Sec. 4.4, respectively. All imagery results shown are rendered at 256^2 resolution.

Training. In all the experiments, we set the learning rate to 5×10^{-5} and decay in every 5,000 iteration with gamma=0.5. We adopt Adam (Kingma and Ba, 2015) optimizer to train the deformation models. In each training iteration, we randomly sample a batch of 10 source NeRFs $\{\mathcal{N}_s^{(i)}\}_{i=1}^{10}$ with corresponding latent codes $\{\mathbf{z}_s^{(i)}\}_{i=1}^{10}$, and a batch of target NeRFs $\{\mathcal{N}_t^{(j)}\}_{j=1}^{10}$ with corresponding latent codes $\{\mathbf{z}_t^{(j)}\}_{j=1}^{10}$. For all experiments, we train the DDF for 80,000 iterations, which takes about 8 hours on a single Tesla V100 GPU. The hyperparameter details are listed in Tab. 1.

Evaluation Dataset. We extensively demonstrate our approach on human faces (Liu et al., 2015) as the main object category, as human faces are rich in geometric details, making them the best choice for demonstrating the accuracy, smoothness, and robustness of learned correspondences. Moreover, human faces are also rich in downstream tasks, from which we can effectively investigate the potential of learned correspondences. The qualitative results on cats (Zhang et al., 2008) and cars (Dosovitskiy et al., 2017; Schwarz et al., 2020) are also included.

Sampling Details. To train the DDF network efficiently, we conduct hierarchical sampling to obtain 3D point sets with more specific semantic meanings. As in (Mildenhall et al., 2020), we first uniformly sample points in 3D space and then sample via importance sampling a more informed fine point set given the density output of the ‘‘coarse’’ point set. These samples are biased toward the more relevant parts of the rendered object. We list the sampling details in Tab. 1. Apart from applying a foreground depth mask to filter out background information to increase sampling efficiency, we also control the sampling ratio of remaining rays. By defining a smaller sampling ratio, we could increase the number of NeRF sampled per batch to increase the diversity of training samples. We curtail the

Table 1 Hyper parameters of the sampling and regularization loss weights.

| Dataset | Ray Steps | Depth Mask | Sampling Ratio | Batch Size | λ_{cycle} | λ_{smooth} |
|------------------------------|-----------|------------|----------------|------------|-------------------|--------------------|
| CelebA (Liu et al., 2015) | 24 | 1.08 | 0.2 | 131,072 | 0.1 | 0.1 |
| Carla (Schwarz et al., 2020) | 48 | 1.2 | 0.05 | 65,536 | 0.05 | 0.01 |
| Cats (Zhang et al., 2008) | 36 | 1.08 | 0.1 | 49,152 | 0.1 | 0.1 |

sampling points to a certain number so to maintain the stability of training.

NeRF-based GANs. We use the officially released π -GAN pretrained models for dense correspondence learning. To extract network features, we use the features starting from layer 4. We find the middle layer features have more correlation with the underlying semantics of a given region, while the last few layers are more sensitive to low-level details such as color variations, which could not provide meaningful clues for dense correspondence learning. We further justify our choice in Fig. 4.5.

4.2 Qualitative Results on Texture Transfer

In this subsection, we qualitatively demonstrate the dense correspondences learned by *DDF* through texture transfer. The results here validate that *DDF* learns accurate underlying structures of NeRFs and their associated correspondences without explicit correspondence supervision provided during training.

Texture Transfer via *DDF*. We denote $\mathcal{N}_s \rightarrow \mathcal{N}_t$ as the process of transferring texture from NeRF \mathcal{N}_s to NeRF \mathcal{N}_t while maintaining the geometry of \mathcal{N}_t . To perform the transfer, for each sampling point \mathbf{x}_s to render NeRF \mathcal{N}_s , we first deform \mathbf{x}_s to the template correspondence \mathbf{x}_0 via B and then deform it to the target NeRF \mathcal{N}_t space correspondence point \mathbf{x}'_t via F . We query the geometry of \mathcal{N}_t and texture of \mathcal{N}_s to conduct volume rendering in the given view direction. To remove ambiguity, we mask out the hair and background class of the source class using segmentation masks and conduct texture transfer on other semantic regions on the human face.

Results on Human Faces. With the above rendering process, we show the cross-instance texture transfer results in Fig. 6. We compare our method with two types of baselines, the model-based 3DMM (Blanz and Vetter, 1999) method (row 1) and the state-of-the-art learning-based 2D correspondence matching methods (Truong et al., 2020a,b, 2021) (rows 2-4). Visually inspected, our method produces semantic plausible dense correspondences with high-fidelity texture transfer results. We also show our results in multiple views to demonstrate

that our method has learned both 3D consistent dense correspondences. Note that good texture transfer results could not be achieved without accurate correspondence matching in 3D space. Our approach shows superior texture transfer in comparison to existing model-based and learning-based methods.

Results on Other Categories. To further illustrate the deformation ability of dual fields in *DDF*, we apply our method on two more pretrained NeRF-based generators, trained respectively on the real-world Cats (Zhang et al., 2008) datasets as well as the synthetic CARLA (Dosovitskiy et al., 2017; Schwarz et al., 2020) dataset. We train the corresponding *DDF* models on the new categories with parameters listed in Tab. 1 and conduct texture transfer using the same pipeline. Given the source NeRF \mathcal{N}_s and target NeRF \mathcal{N}_t , we show transfer results from both $\mathcal{N}_s \rightarrow \mathcal{N}_t$ and $\mathcal{N}_t \rightarrow \mathcal{N}_s$ to validate the performance of *DDF* on shape categories with larger structure variations.

In Fig. 7 we show the texture transfer results on the Cats dataset. Though cat’s faces have fewer discriminative features compared to human faces, through the overall shape and local details such as the size of the cat’s eye and mouth, we could see that the transferred multi-view results share the same texture with the source NeRF, while still matching the geometry of the target NeRF.

In Fig. 8 we show the transfer results on synthetic CARLA dataset. Compared to CelebA and Cat datasets, Cars have larger structure variations and larger deformations between different NeRFs, leaving learning accurate deformation on CARLA dataset more challenging. Through the qualitative results, the texture transfer of $\mathcal{N}_s \rightarrow \mathcal{N}_t$ through *DDF* produces convincing correspondence across two NeRFs that are largely different. The shared semantic components are matched to the maximum extent and also preserve the original geometry pattern of NeRF \mathcal{N}_t . The texture transfer of the other direction $\mathcal{N}_t \rightarrow \mathcal{N}_s$ is overall reasonable but produces mismatches in some regions with large deformations such as the car roof, whose size varies evidently across different objects represented in NeRFs.

Uncertainty of Texture Transfer. In Fig. 9 we showed the uncertainty heat map and the texture trans-

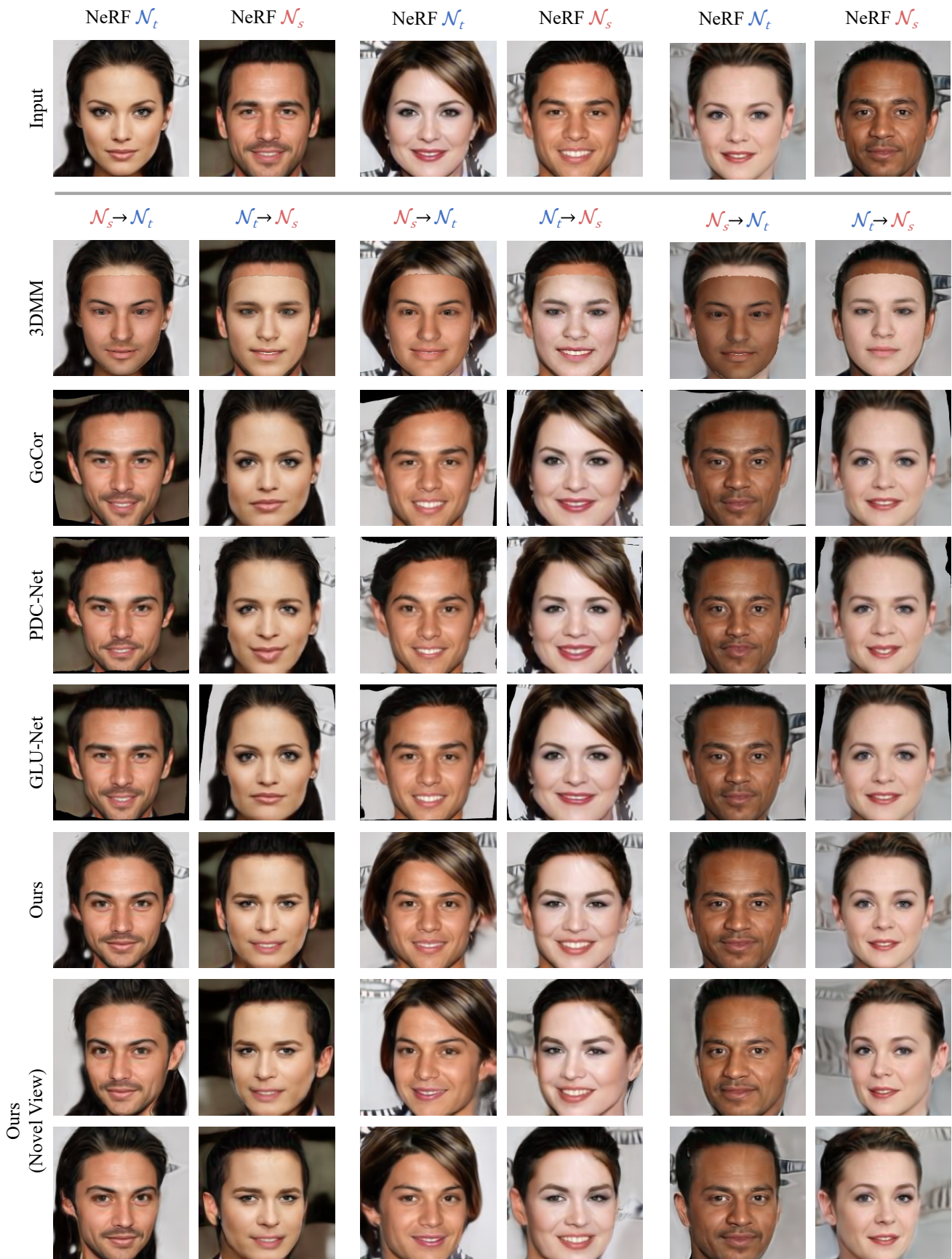


Fig. 6 Texture transfer through the learned deformation field. We randomly sample three NeRF pairs here for qualitative evaluation (shown at the top row as inputs). For each NeRF sample \mathcal{N}_* we transfer the texture from the paired NeRF according to their 3D dense correspondences. Specifically, for the column labeled with NeRF $\mathcal{N}_{t(s)}$, we show the texture transfer results from source NeRF $\mathcal{N}_{s(t)} \rightarrow \mathcal{N}_{t(s)}$. We conduct dual texture transfer on three pairs (depicted in different separated columns) and show the transferred results over three different angles. The separate line splits the input, the model-based method’s output, the learning-based methods’ output, and ours. Though not designed for 2D images, our method consistently outperforms the baseline method in terms of fidelity and naturalness.

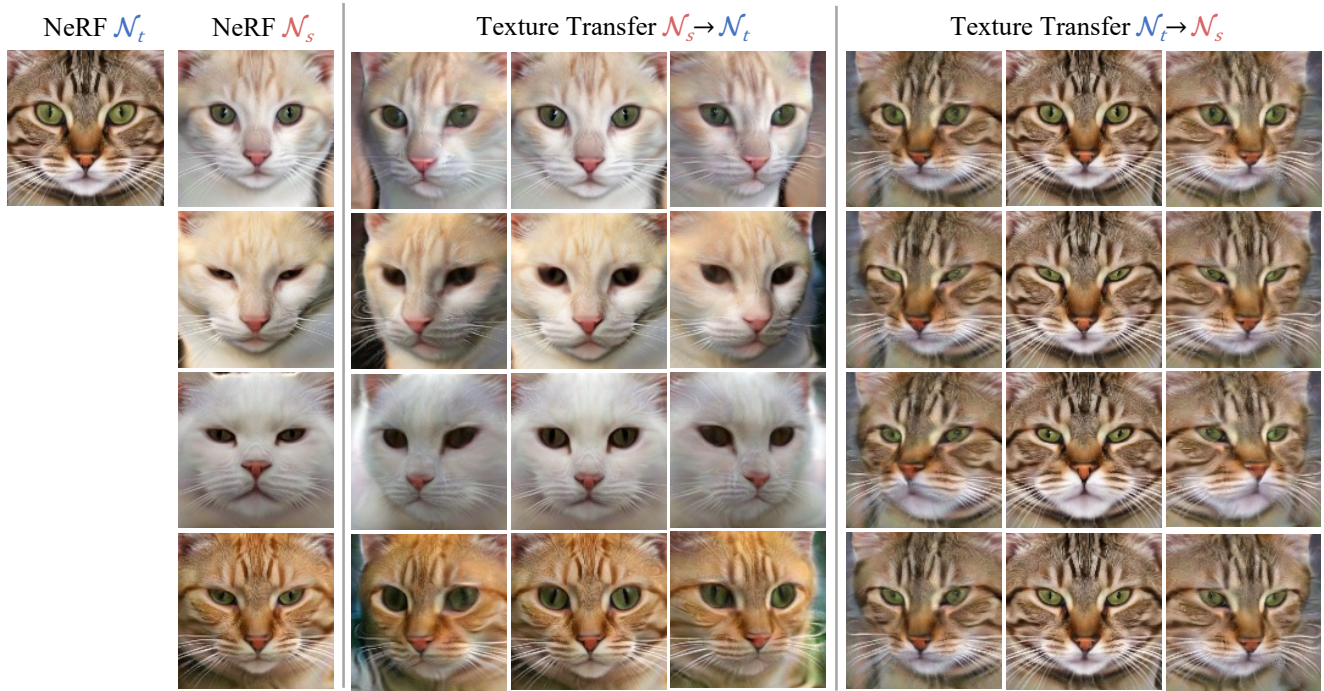


Fig. 7 Visualization of texture transfer on Cats Dataset. The size of the eyes and positions of the nose and the overall shape could serve as hints to observe the difference between different cats.

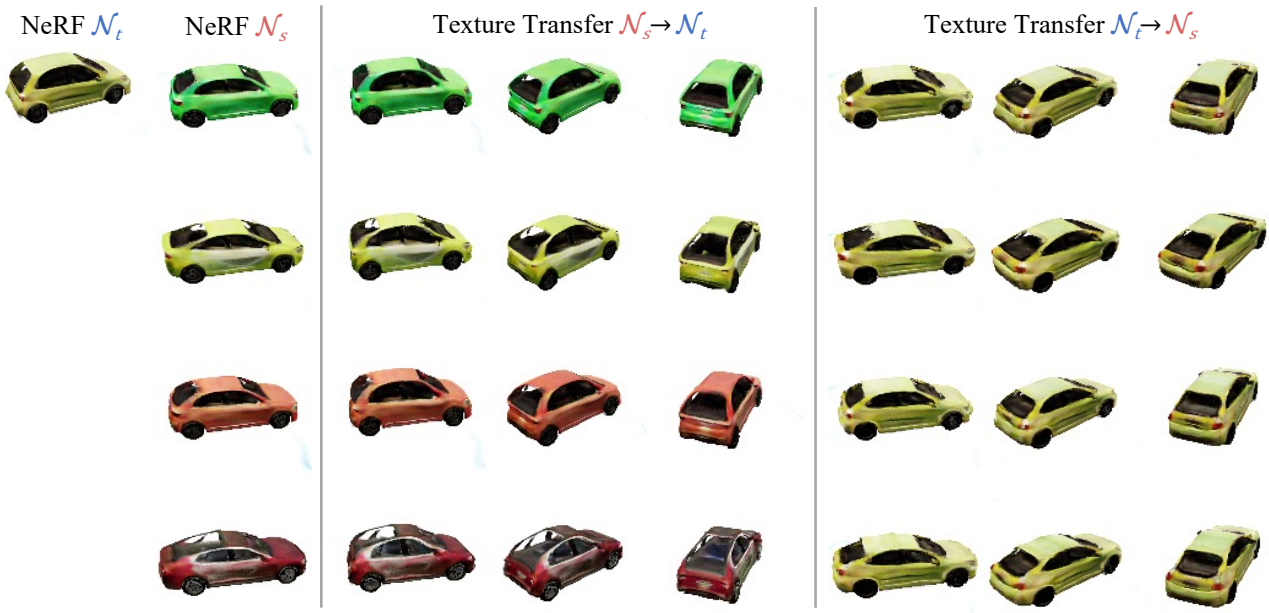


Fig. 8 Visualization of texture transfer on CARLA Dataset. In the category with large structure deviations, *DDF* could still generate sound deformation with high fidelity and accuracy.

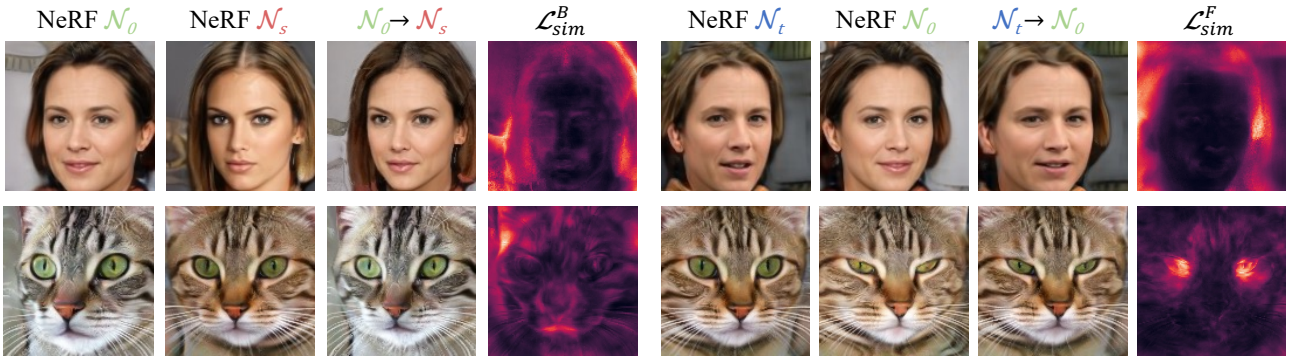


Fig. 9 Visualization of uncertainty map of learned dense correspondence. The left and the right column shows the pixel-wise uncertainty map corresponding to backward deformation B and forward deformation F , respectively. The pixel-wise uncertainty is calculated as the integration of the point-wise \mathcal{L}_{sim}^* with Eq. 1.

fer results of the learned DDF . After the training of DDF , we conduct correspondence inference and calculate the feature similarity loss of the correspondence points and the original points. The feature similarity loss \mathcal{L}_{sim}^B and \mathcal{L}_{sim}^F between inferred correspondence points could be naturally interpreted as the uncertainty of the learned correspondence. A low feature similarity loss denotes the correctness of deformation and guarantees the visual effects of texture transfer. In Fig. 9, we separately show the uncertainty maps corresponding to the backward deformation B and the forward deformation F . As can be seen, the semantic regions of the human face have a low uncertainty score, except for ambiguous regions like hair. For Cat face, the overall uncertainty is low except for the regions where deformations are large such as cat eyes and mouth. After DDF converges, the heat map could also serve as the confidence score of the dense correspondences between two NeRFs.

4.3 Quantitative Results on Segmentation Label Propagation

To demonstrate the quantitative performance of the learned dense correspondence, following the previous method (Deng et al., 2021) we resort to segmentation label propagation as the surrogate metric. Intuitively, a 3D point shall share the same segmentation label with its correspondence point from another object with structure variations if being deformed via an accurate correspondence algorithm. Thus, segmentation label propagation could serve as a metric to inspect the performance of learned correspondences. Similar to the texture transfer experiments discussed in Sec. 4.2, here we conduct segmentation label propagation on the fine-grained human faces.

Different from explicit-based representations and SDF-based implicit representation (Deng et al., 2021; Park et al., 2019; Zheng et al., 2021), NeRF-based representation is designed for view synthesis and has no clear surface boundary, leaving it hard to directly evaluate the segmentation accuracy in the 3D space. Therefore, we propose to conduct segmentation label propagation in the 3D space and project the propagated labels in the 2D space through volume rendering depicted in Eq. 1 for evaluation. We describe how we conduct segmentation label propagation below.

Segmentation Label Propagation. For this task, we first render the front view of our template NeRF \mathcal{N}_0 and provide it with the oracle segmentation map acquired from a pretrained DeepLabV3 (Chen et al., 2017; Zhang et al., 2021b) segmentation model. We refer to this front view as the oracle image, as shown in Fig. 10(b). For an unlabeled test image rendered from a NeRF, for each pixel, we cast a ray through this pixel and sample 96 points along the corresponding ray. For a point \mathbf{x} along the ray, we use the network B to query its correspondence point \mathbf{x}' in the template NeRF. The projected segmentation label is thus regarded as the segmentation label prediction of \mathbf{x} . To acquire 2D segmentation predictions for evaluation, we aggregate the predictions of 3D points by rescaling their voting contributions with the transmittance value $T(i)$ defined in Eq. 1. The whole segmentation process costs around 3 seconds for a single image on a Tesla V100 GPU.

Since we only use the oracle segmentation map for the oracle image, we consider our approach as a 1-shot segmentation method.

Evaluation Settings. We compare DDF with DatasetGAN (Zhang et al., 2021b) and CoordGAN (Mu et al., 2022), which are respectively the state-of-the-art 2D GAN-based few-shot segmentation method and the concurrent work on establishing

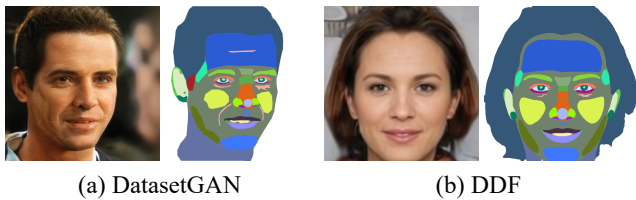


Fig. 10 Canonical segmentation annotation for two 1-shot segmenters. (a) DatasetGAN (Zhang et al., 2021b) and (b) ours. For DatasetGAN we choose the first annotated image in their training set, and for *DDF* we simply use the frontal face of the Template for segmentation transfer. For ease of comparison, the segmentation annotations of the Template are simply acquired through an off-the-shelf pretrained DatasetGAN segmenter, which already provides reasonable results.

2D correspondences via 2D GANs. We also include the 2D representation learning baselines from CoordGAN for reference.

Since *DDF* does not directly accept real images as input, following Zhang et al. (2021b), we sample 10,000 image-annotation pairs from pretrained GANs as a dataset and train a segmentation model, as shown in Fig. 11. We evaluate the trained segmentation model on the official DatasetGAN test set to quantify the segmentation accuracy, which consists of 16 fine-grained annotated 1024^2 real-world images. For a fair comparison, we also train an 1-shot DeepLabV3 model as the baseline, which uses one annotated pair as the sampling source (Fig. 10(a)) and follows the data generation pipeline of Zhang et al. (2021b). Since Zhang et al. (2021b) adopts pretrained StyleGAN under 512^2 resolution on the FFHQ dataset while our pretrained GANs are trained over 128^2 resolution CelebA dataset, all the test images are bilinear interpolated with a resolution of 256^2 for evaluation. We adopt the official implementation of DatasetGAN for data generation and use the default settings for all the segmentation models training. The standard mIOU is adopted as the segmentation evaluation metric.

Results. We show the quantitative results the test set of Zhang et al. (2021b) in Tab. 2. As can be seen, our method achieves comparable performance with the baseline, and even performs better over some classes like hair and nose, indicating that our learned correspondences are accurate and smooth. We show the qualitative results in Fig. 12. As can be observed, without relying on explicit segmentation supervision, our method can perform 3D consistent segmentation transfer, which is not possible with existing 2D correspondence baselines such as DatasetGAN 1-shot segmenter. This is made possible by establishing plausible correspondence between different semantic regions across NeRFs, despite their structure variations in 3D space.

For further comparison with concurrent work that distills correspondences from 2D GANs, Tab. 3 presents the mIOU scores over two real-world datasets. Following Mu et al. (2022), we train an encoder that predicts the source NeRF code \mathbf{z}_s using the techniques described in Sec. 4.6 and conducts feed-forward inference over the input images. Our method outperforms 2D learning-based models on this task and achieves competitive performance compared with CoordGAN, with the merit of establishing dense correspondences in 3D space. Compared with building correspondences over 2D pixels, establishing correspondences in implicit 3D space is exponentially harder, as explained in Sec. 1. Moreover, compared with mature 2D GAN families and toolboxes, the development of 3D GANs is still in its early stage. Equipping *DDF* with more developed 3D GANs, *i.e.* Chan et al. (2022), can potentially close the gap.

4.4 Quantitative Results on Keypoints Transfer

Though segmentation label propagation is an intuitive and well-adopted surrogate metric for evaluating learned correspondence, we argue that quantitative evaluation using this metric alone is contrived. Specifically, segmentation label propagation is essentially a pixel-wise classification task, which means any errors in dense correspondences within a segment will not be detected. Moreover, only network *B* is used in the segmentation label propagation experiment, which could not quantitatively evaluate the forward deformation field *F* in our method. Therefore, we further evaluate our method via keypoints transfer (Zheng et al., 2021), which is a regression task with independent ground truth for each transferred landmark. In our context, this task can be viewed as few-shot 3D facial landmark transfer learning with 1 sample as training data.

For this task, as in the segmentation label propagation pipeline, we first use an off-the-shelf facial landmarks prediction model (Wang et al., 2019a) to label the template frontal view image with 98 landmarks, which can be seen in the middle of Fig. 13. Since these points are in the image space, we first unproject them back to the template NeRF 3D space by appending the corresponding depth values viewing these landmarks positions, which we denote as $\mathcal{P}_0^{lms} = \{\mathbf{x}_0^{lms(k)}\}_{k=1}^{98}$. After that, we resort to *F* model and deform these unprojected 3D points to \mathcal{N}_t by $F(\mathbf{x}_0^{lms(*)}, \mathbf{z}_t) = \mathbf{x}_t^{lms(*)}$. The deformed points $\mathbf{x}_t^{lms(*)}$ are projected back to the image space as the transferred 2D facial landmarks of \mathcal{N}_t .

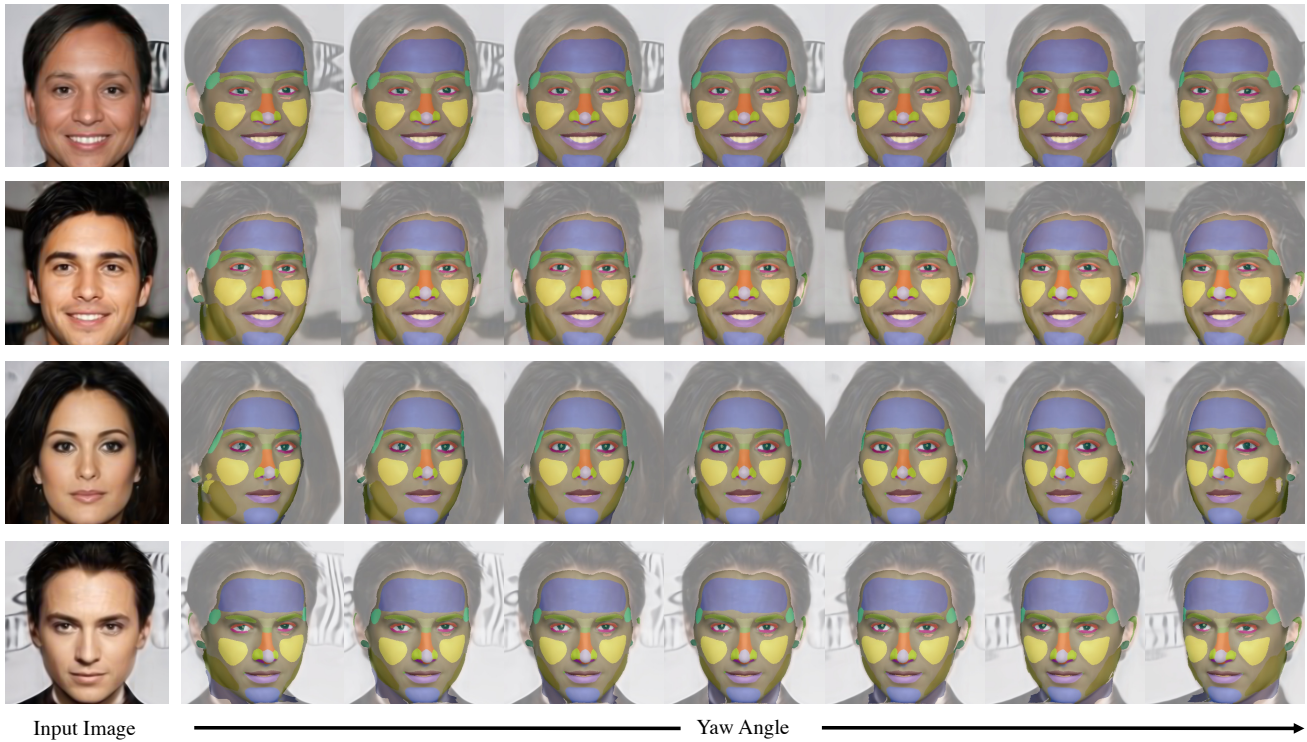


Fig. 11 3D consistent segmentation label transfer with novel poses. Given an annotated projection of Template NeRF shown in Fig. 10(b), we could derive view-consistent segmentation maps of other NeRF objects through our method. Note that for instances missing teeth class (1st row and 2nd row, segment in white color), our method could still derive accurate correspondences though the teeth class does not exist in the segmentation template. This demonstrates that our method learns consistent 3D dense correspondence.

Table 2 mIOU scores of two 1-shot segmenters on DatasetGAN (Zhang et al., 2021b) test set. The corresponding segmenters are trained over the synthetic dataset generated by two methods. We show the performance of two versions of *DDF* based on two generators pretrained on different datasets. The 1-shot segmenter trained on our dataset is competitive against the counterpart which is trained in high-resolution images, demonstrating the merit of the learned correspondence.

| Method | Mean IOU | Eyes | Mouth | Nose | Cheek | Chin | Hair | Eyebrows | Ears | Jaw | BG |
|-----------------------------|-------------|-------------|-------------|-------------|-------------|-------------|-------------|-------------|-------------|-------------|-------------|
| DatasetGAN 1-shot segmenter | 56.9 | 40.5 | 62.6 | 52.5 | 61.6 | 65.5 | 72.4 | 59.6 | 49.0 | 16.4 | 81.4 |
| <i>DDF</i> 1-shot segmenter | 54.6 | 51.0 | 53.2 | 55.4 | 69.2 | 82.6 | 67.4 | 54.2 | 40.9 | 66.9 | 75.06 |

Evaluation Settings We also compare our method with both 3D model-based method (3DMM (Blanz and Vetter, 1999)) as well as current state-of-the-art 2D learning-based matching method (Truong et al., 2020a,b, 2021) as our baselines. We regard the output of a representative landmark detector MTCNN (Zhang et al., 2016) as ground-truth. For baselines, we also consider the hand-crafted descriptor SIFT Flow (Liu et al., 2011) as well as several learned descriptors (Truong et al., 2020a,b, 2021) that attain state-of-the-art performance on commonly used dense correspondence benchmarks (*e.g.*, MegaDepth (Li and Snavely, 2018)). For the baselines, we use the officially released models to conduct inference in our experiments. We employ the

Percentage of Correctly Keypoints (PCK) and Average End Point Error (AEPE) as the evaluation metrics.

Results. We evaluate the performance over 5,000 randomly sampled human faces with different view angles and show the quantitative results in Tab. 4. At threshold PCK@0.01, *DDF* achieves 41.6 against competitive baselines. This result strongly supports the effectiveness of *DDF*.

4.5 Ablation Study

Selection of Generator Feature. In our work, we select multiple layers from the generator as the training supervisions of the feature similiary losses depicted

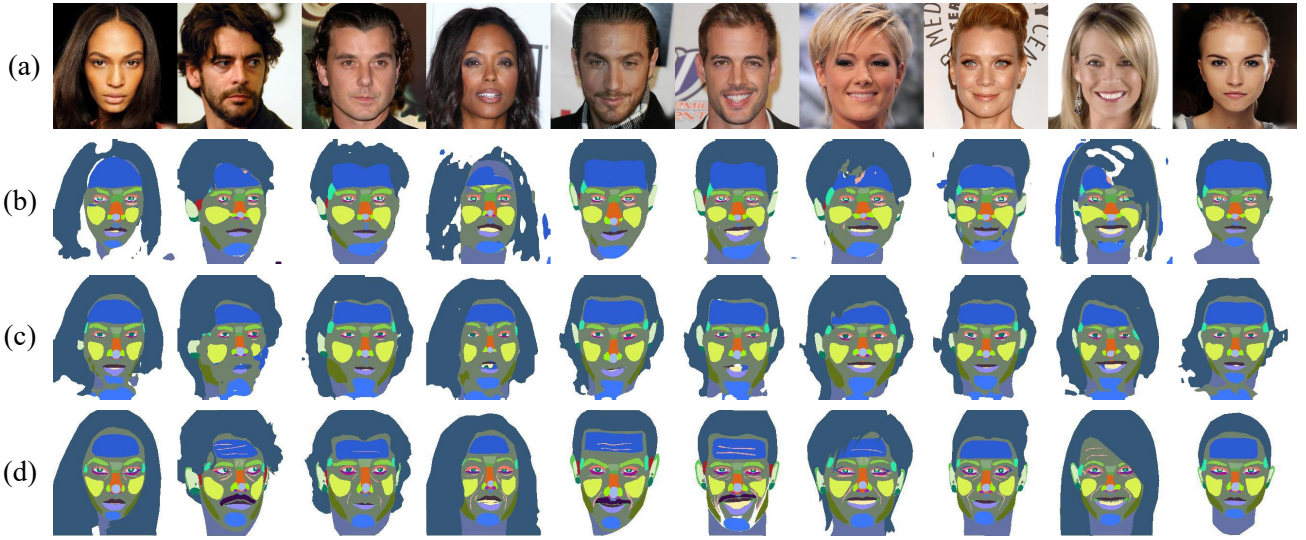


Fig. 12 Visualization of the 1-shot segmenter prediction. Starting from the top row, we show the (a) The test set input image, (b) segmentation prediction from DatasetGAN 1-shot segmenter, (c) segmentation prediction from DDF1-shot segmenters and (d) the ground truth segmentation annotation.

Table 3 IOU comparison for segmentation label propagation. Our method achieves comparative performance with the 2D representation learning method, and is the only method that supports 3D dense correspondence searching over implicit functions. * means 3D aware.

| Method | CelebA-HQ | DGAN-face |
|---|-----------|-----------|
| Swap AE (Park et al., 2020) | 24.73 | 5.48 |
| MoCo (He et al., 2019) | 36.19 | 10.00 |
| VFS (Xu and Wang, 2021) | 38.10 | 8.55 |
| ResNet50 (He et al., 2016) | 39.48 | 11.05 |
| DDF* | 45.32 | 19.18 |
| Pix2Style2Pix (Richardson et al., 2021) | 48.50 | 20.36 |
| CoordGAN (Mu et al., 2022) | 52.25 | 23.78 |

Table 4 PCK-Transfer on facial landmarks. Our method achieves better performance compared to both model-based (row 2) and learning-based (rows 3,4,5) methods.

| Methods | Correspondence Supervision | PCK@0.05 \uparrow | PCK@0.01 \uparrow | AEPE \downarrow |
|--------------------------------|----------------------------|---------------------|---------------------|-------------------|
| SIFT Flow (Liu et al., 2011) | - | 92.7 | 32.9 | 5.22 |
| PDC-Net (Truong et al., 2021) | matching image pairs | 89.1 | 26.8 | 6.28 |
| GoCor (Truong et al., 2020a) | matching image pairs | 87.9 | 24.8 | 6.24 |
| GLU-Net (Truong et al., 2020b) | matching image pairs | 90.0 | 30.4 | 5.78 |
| Ours | GAN-supervised | 95.0 | 41.6 | 4.47 |

in Eq. 5 and 6. Here we justify the intuition behind this. Different from the feed-forward models (He et al., 2016; Simonyan and Zisserman, 2015), generative models like GANs is trained to decode information from a compact latent code. Therefore, features from earlier layers should contain more high-level semantics information while later layers contain more instance-specific texture information. To justify this intuition, we show

the layer-wise feature similarity heatmap between the projected 2D feature maps of \mathcal{N}_s and \mathcal{N}_t over a pre-trained π -GAN generator in Fig. 14. Specifically, given \mathcal{N}_s and \mathcal{N}_t , we calculate the 2D feature maps by integrating the features of points along each rays using the volume rendering equation depicted in Eq. 1 and get two sets of features maps $F_s = \mathcal{R}^{N*H*W*C}$ and $F_t = \mathcal{R}^{N*H*W*C}$, where $N = 9$ is the layer number

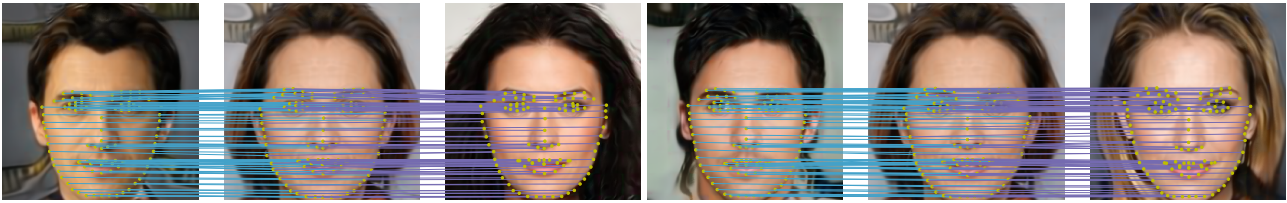


Fig. 13 Visualization of learned correspondences via landmark transfer. For each triplet, we first predict 98 facial landmarks of the first column acquired through an off-the-shelf model (Wang et al., 2019a). We deform the predicted landmarks to the template through network B , and then further deform the landmarks on the template to another sampled face through network F . We sample 3D points near the surface of one NeRF and calculate the dense correspondence point on the target NeRF with our deformation network. Please zoom in for details.

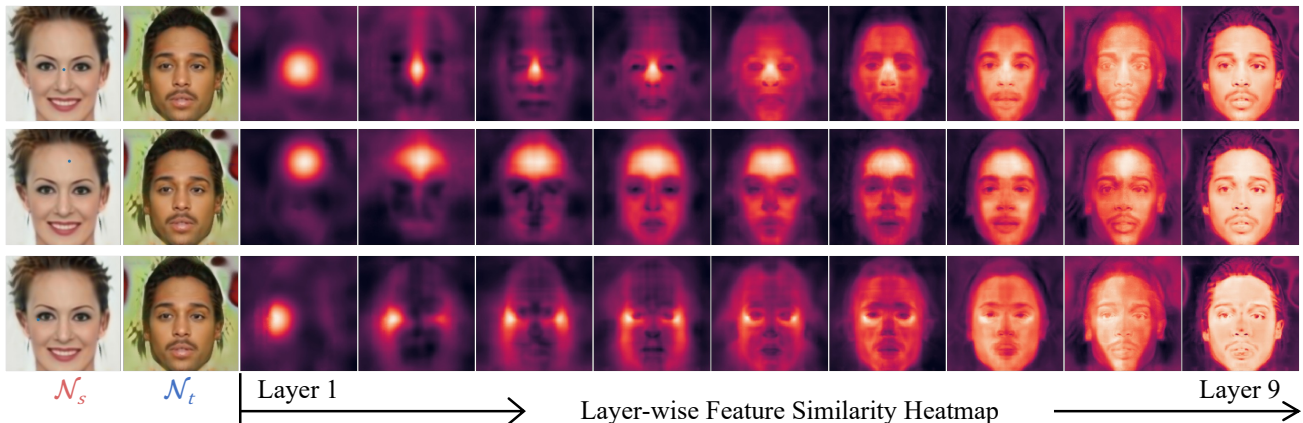


Fig. 14 Layer-wise feature correlation between projected features of two NeRF. The NeRFs are sampled from a pretrained π -GAN generator from *shallow* (leftmost) to *deep* (rightmost). Since π -GAN generator adopts an 8-layer MLP design appended with a view-dependent MLP layer, here from left to right, we show the feature similarity heatmap from the 1st layer (3rd column) to the 9th layer (last column) of the pretrained generator. We project the features of 3D NeRF to 2D using Eq. 1 for better visualization. In each row, a random 2D point from the source NeRF is selected to calculate layer-wise feature similarity heatmaps with the projected feature map of the target NeRF.

of π -GAN generators. Given a 2D coordinate (u, v) , we retrieve its corresponding features $F_s^{u,v} \in \mathcal{R}^{N \times C}$ from the source feature maps F_s and calculate the cosine similarity with the target feature maps F_t within each layer.

As can be seen, the generator features from different layers encode semantics from different levels, where the semantics compactness linearly decreases as the network goes deeper. Surprisingly, the early generator features are even robust under the symmetric semantics such as the right and left corners of the eyes (3rd row). This is an indispensable property in establishing dense correspondences where a 3D point from the source left eye should not establish correspondence to points in the right eye region of the target. Thus, we choose the normalized features from the first 5 layers as the supervision signals of the DDF , which encode unambiguous correspondence information. This property has also been validated in 2D generative models (Peebles et al., 2022; Yang et al., 2022; Zhang et al., 2021a), where dif-

ferent layers of pretrained StyleGAN encode different types of information.

Deformation Regularization Terms. We validate the efficacy of our regularization terms in terms of qualitative results, including the cycle consistency term and deformation smoothness term. To construct a baseline for evaluation, we remove the correspondence deformation smoothness loss term and only apply supervision from the feature similarity loss on network training. To evaluate the effect of cycle consistency regularization, we train a baseline without cycle consistency loss term and visualize the self-reconstruction as well as texture transfer results using the trained dual deformation field. As shown in Fig. 15(a), cycle-consistency term encourages the consistency property, that after the forward and backward deformation a point from the source shape will map to itself. Meanwhile, the model trained with cycle consistency term learns less noisy deformation, which is essential when conducting downstream tasks such as texture transfer. As shown in Fig. 15(b), without the deformation smoothness regularization, the

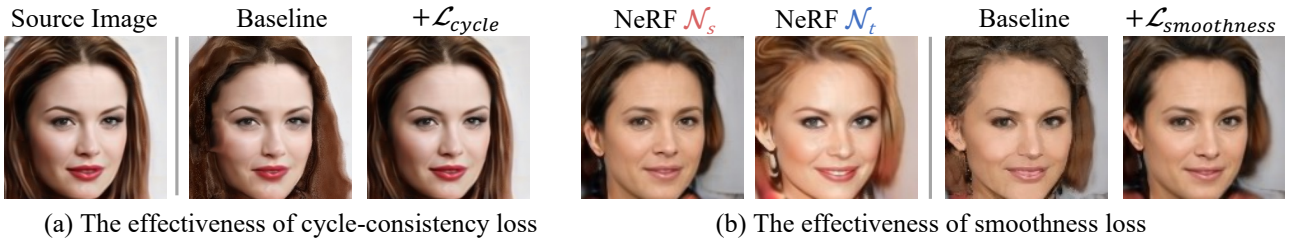


Fig. 15 (a) **Rendering from the self-reconstructed point through cycle deformation.** From the left is the input image, reconstructed with and without cycle-consistency loss. The deformation model trained with cycle-consistency loss can perfectly reconstruct itself, while the one without cycle-consistency loss leads to distortions. (b) **Output from deformation network trained without and with deformation smoothness loss.** We demonstrate the effectiveness of L_{smooth} via texture transfer from A to B . The lack of smoothness regularization leads to distorted visual results. Better zoom in for a better experience.

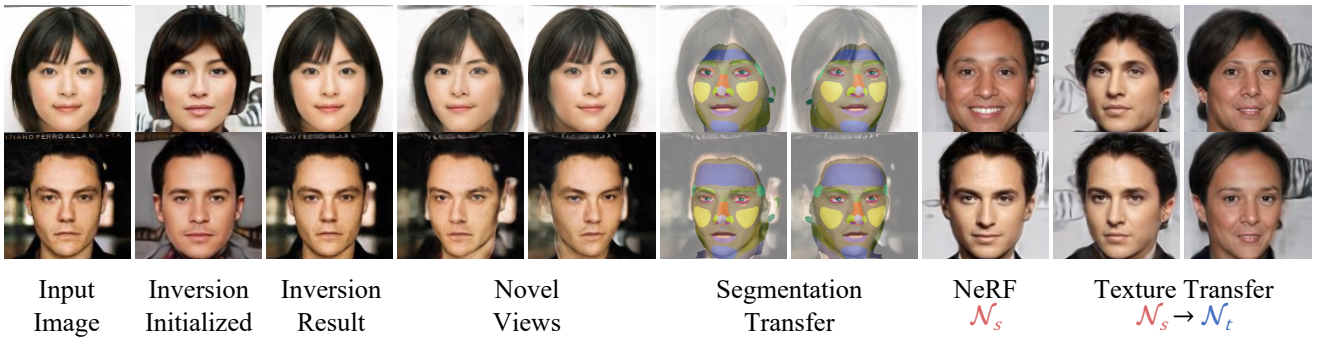


Fig. 16 **Extending DDF to real images.** To apply DDF to real-world image, we first invert the real-world images (1st column) into the latent space of the 3D GAN (2nd and 3rd columns). Beyond novel view synthesis (4th and 5th columns), DDF also supports 3D consistent segmentation transfer (6th and 7th columns). Given the reference NeRFs (8th column), our method could edit the texture of given identities without changing the overall shape.

network tends to learn noisy deformation which leads to distortions in the final rendering. For the second order cycle consistency regularization, we find it has similar effect with \mathcal{L}_{cycle} in qualitative performance. Moreover, we set $\lambda_{cycle}^{2nd} = 0$ and conduct the segmentation transfer evaluation as in Tab. 2 and observe a mIOU degrade from 56.9 to 55.3, which validates $\mathcal{L}_{cycle}^{2nd}$ could improve the deformation field performance.

Curriculum Training. To show that our proposed curriculum training strategy could help regularize the training and facilitate convergence, we report the values of feature similarity loss over the evaluation set, with different curriculum steps adopted during training. Using 16/128/1024/4096 steps the loss are respectively 0.455/0.410/0.310/0.287, which demonstrates the effectiveness of our method.

4.6 Extending DDF to Real Images

Training An Encoder for Inversion. To apply DDF real-world images, we use two encoders, namely

an encoder denoted by $E(\cdot, \theta_G)$ to invert the input image to the latent space of the NeRF-based GAN and another encoder represented by $E(\cdot, \theta_{DDF})$ to invert the input image to the deformation conditions. Specifically, rather than directly output the low-dimensional deformation code \mathbf{z} , here we follow the observations of [Tov et al. \(2021\)](#) which project the \mathcal{Z} -space code \mathbf{z} to the $\mathcal{W}+$ space for better performance. Since the NeRF-based GAN (*i.e.*, π -GAN) already follows this design, here we further augment each of the deformation fields with a mapping function \mathcal{M}_{DDF} ([Chan et al., 2021c](#); [Sitzmann et al., 2020](#)). During inversion, the corresponding encoders directly output the $\mathcal{W}+$ space modulations, *i.e.*, $E(I, \theta_G) = \beta_G^I, \gamma_G^I$ and $E(I, \theta_{DDF}) = \beta_{DDF}^I, \gamma_{DDF}^I$.

The encoders are trained in two stages. In the first stage, we train the encoder $E(\cdot, \theta_G)$ where the output latent codes β_G^I, γ_G^I are fed into the NeRF-based GAN to render a replicate of the images $\hat{I} = G(\beta_G^I, \gamma_G^I, \xi_I)$, where ξ_I is the estimated camera pose of the input image using an off-the-shelf pose estimator. After $E(\cdot, \theta_G)$



Fig. 17 Mask-guided texture transfer over real cases. In the second column, we show the projected image of the GAN inversion of the source image. For mask-guided texture manipulation, we sample two synthetic NeRF from the pretrained GAN (4th and 7th columns) and conduct texture transfer guided by the foreground mask.

converges, in the second stage we train the encoder $E(\cdot, \theta_D)$ to output the corresponding deformations conditions β_B^I, γ_B^I and β_F^I, γ_F^I . Given the inverted latent code β_G^I, γ_G^I of the input image, we conduct self texture transfer described in Sec. 4.2 to replicate the input image. To stabilize training, we also include synthetic samples from the pre-trained NeRF GAN as training data. Given a latent code $z \sim p_z$, we get the paired modulations β_z, γ_z and synthesized image $I_z = G(z, \xi)$ under a random camera pose $\xi \sim p_\xi$ as training samples. Apart from image reconstruction loss, the predicted modulations from $E(\cdot, \theta_D)$ are encouraged to mimic the synthetic ground truth. We find the synthetic latent code regularization could stabilize the deformation encoder training. Following [Tov et al. \(2021\)](#), the encoders predict the offsets of the mean modulations of the corresponding mapping function $\beta_0^{DDF}, \gamma_0^{DDF}$ for better initialization. The overall training objectives are: 1) *Image Reconstruction Loss*: We utilize the pixel-wise \mathcal{L}_2 as well as the LPIPS loss \mathcal{L}_{LPIPS} ([Zhang et al., 2018](#)) as the image reconstruction supervisions:

$$\mathcal{L}_{image} = \mathcal{L}_2(I, G(E(I, \theta_G), \xi_I)) + \mathcal{L}_{LPIPS}(I, G(E(I, \theta_G), \xi_I)), \quad (12)$$

2) *Latent Codes Regularization*: We regularize the encoded latent codes to match the pseudo ground truth latent codes distribution:

$$\mathcal{L}_{latent} = \mathcal{L}_2((\beta_z, \gamma_z), E(I_z, \theta_D)). \quad (13)$$

Results. Here we show the texture transfer results over real images in Fig. 16. As can be seen, our hybrid inversion method could faithfully reconstruct the given real images without affecting the view synthesis ability of NeRF. Furthermore, with *DDF*, accurate 3D-consistent segmentation transfer and faithful texture transfer become possible, which is beyond the reach of existing 2D methods. We further show a mask-guided texture transfer applied over real cases in Fig. 17, which shows the potential of our method over real-world applications beyond basic texture transfer and segmentation labeling.

5 Conclusion

In this work we propose to leverage a pre-trained NeRF-based GAN, π -GAN in our case, to build dense correspondence between NeRF representations of different objects within the same category. The key insight is that the pre-trained GAN possesses three important properties that can help alleviate the challenges of this task, namely 1) instance-specific latent codes that holistically capture the global structure of different NeRFs, 2) geometric-aware generator features that reflect local geometric details of different NeRFs, and 3) the manifold of NeRFs that serves as a source of infinite NeRF samples. Based on the three properties, we respectively propose a generalizable model, referred to as Dual Deformation Field, a learning objective based on generator features that approximate geometric distances in feature space, and finally an effective curriculum training strategy that feeds samples with growing complexity. To the best of our knowledge, this is the first method that tries to establish dense correspondence across NeRF representations. Our experiments demonstrate that dense correspondences between NeRFs learned from our framework are accurate, smooth, and robust, making them applicable in various downstream applications.

Data Availability. The datasets that support the findings of this study are all publicly available for the research purpose.

References

- Bau D, Zhu JY, Strobel H, Lapedriza A, Zhou B, Torralba A (2020) Understanding the role of individual units in a deep neural network. PNAS DOI 10.1073/pnas.1907375117, URL <https://www.pnas.org/content/early/2020/08/31/1907375117>
- Blanz V, Vetter T (1999) A morphable model for the synthesis of 3d faces. In: SIGGRAPH
- Brock A, Donahue J, Simonyan K (2019) Large scale GAN training for high fidelity natural image synthesis. In: ICLR, OpenReview.net, URL <https://openreview.net/forum?id=B1xsqj09Fm>
- Chan E, Monteiro M, Kellnhöfer P, Wu J, Wetzstein G (2021a) pi-gan: Periodic implicit generative adversarial networks for 3d-aware image synthesis. In: CVPR
- Chan ER, Lin CZ, Chan MA, Nagano K, Pan B, Mello SD, Gallo O, Guibas L, Tremblay J, Khamis S, Karras T, Wetzstein G (2021b) Efficient geometry-aware 3D generative adversarial networks. In: arXiv
- Chan ER, Monteiro M, Kellnhöfer P, Wu J, Wetzstein G (2021c) pi-GAN: Periodic implicit generative adversarial networks for 3D-aware image synthesis. In: CVPR
- Chan ER, Lin CZ, Chan MA, Nagano K, Pan B, Mello SD, Gallo O, Guibas L, Tremblay J, Khamis S, Karras T, Wetzstein G (2022) Efficient geometry-aware 3D generative adversarial networks. In: CVPR
- Chang AX, Funkhouser T, Guibas L, Hanrahan P, Huang Q, Li Z, Savarese S, Savva M, Song S, Su H, Xiao J, Yi L, Yu F (2015) ShapeNet: An Information-Rich 3D Model Repository. Tech. Rep. arXiv:1512.03012 [cs.GR], Stanford University — Princeton University — Toyota Technological Institute at Chicago
- Chen LC, Papandreou G, Schroff F, Adam H (2017) Rethinking atrous convolution for semantic image segmentation. arXiv abs/1706.05587
- Chen Z, Zhang H (2019) Learning implicit fields for generative shape modeling. In: CVPR, pp 5932–5941
- Deng Y, Yang J, Tong X (2021) Deformed implicit field: Modeling 3d shapes with learned dense correspondence. In: CVPR, pp 10286–10296
- Dosovitskiy A, Ros G, Codevilla F, Lopez A, Koltun V (2017) Carla: An open urban driving simulator. In: Proc. CoRL
- Dumoulin V, Perez E, Schucher N, Strub F, Vries Hd, Courville A, Bengio Y (2018) Feature-wise transformations. Distill DOI 10.23915/distill.00011, <https://distill.pub/2018/feature-wise-transformations>
- Egger B, Smith W, Tewari A, Wuhler S, Zollhöfer M, Beeler T, Bernard F, Bolkart T, Kortylewski A, Romdhani S, Theobalt C, Blanz V, Vetter T (2020) 3d morphable face models—past, present, and future. TOG 39:1 – 38
- Eisenberger M, Novotný D, Kerchenbaum G, Labatut P, Neverova N, Cremers D, Vedaldi A (2021) Neuro-morph: Unsupervised shape interpolation and correspondence in one go. In: CVPR
- Eslami SMA, Rezende DJ, Besse F, Viola F, Morcos AS, Garnelo M, Ruderman A, Rusu AA, Danihelka I, Gregor K, Reichert DP, Buesing L, Weber T, Vinyals O, Rosenbaum D, Rabinowitz NC, King H, Hillier C, Botvinick MM, Wierstra D, Kavukcuoglu K, Hassabis D (2018) Neural scene representation and rendering. Science 360:1204 – 1210
- Fan Z, Hu X, Chen C, Peng S (2019) Boosting local shape matching for dense 3d face correspondence. In: CVPR, pp 10936–10946
- Gafni G, Thies J, Zollhöfer M, Nießner M (2021) Dynamic neural radiance fields for monocular 4d facial avatar reconstruction. In: CVPR, pp 8649–8658
- Goodfellow IJ, Pouget-Abadie J, Mirza M, Xu B, Warde-Farley D, Ozair S, Courville AC, Bengio Y (2014) Generative adversarial nets. In: NIPS
- Gu J, Liu L, Wang P, Theobalt C (2022) Stylen-erf: A style-based 3d aware generator for high-resolution image synthesis. In: ICLR, URL <https://openreview.net/forum?id=iUuzzTMUw9K>
- Guo Y, Chen K, Liang S, Liu Y, Bao H, Zhang J (2021) Ad-nerf: Audio driven neural radiance fields for talking head synthesis. In: ICCV
- Halimi O, Litany O, Rodola E, Bronstein AM, Kimmel R (2019) Unsupervised learning of dense shape correspondence. In: CVPR, pp 4370–4379
- He K, Zhang X, Ren S, Sun J (2016) Deep residual learning for image recognition. In: CVPR
- He K, Fan H, Wu Y, Xie S, Girshick R (2019) Momentum contrast for unsupervised visual representation learning. arXiv
- Hong Y, Peng B, Xiao H, Liu L, Zhang J (2022) Head-nerf: A real-time nerf-based parametric head model. In: CVPR
- Jahani A, Chai L, Isola P (2020) On the "steerability" of generative adversarial networks. In: ICLR
- Kaick OV, Zhang H, Hamarneh G, Cohen-Or D (2011) A survey on shape correspondence. Computer Graphics Forum 30
- Karras T, Laine S, Aila T (2019a) A style-based generator architecture for generative adversarial networks. In: CVPR, pp 4396–4405
- Karras T, Laine S, Aila T (2019b) A style-based generator architecture for generative adversarial networks. In: CVPR

- Kingma DP, Ba J (2015) Adam: A method for stochastic optimization. In: ICLR, vol abs/1412.6980
- Li Z, Snavely N (2018) Megadepth: Learning single-view depth prediction from internet photos. In: ICCV, pp 2041–2050
- Li Z, Niklaus S, Snavely N, Wang O (2021) Neural scene flow fields for space-time view synthesis of dynamic scenes. In: CVPR
- Litany O, Remez T, Rodolà E, Bronstein A, Bronstein M (2017) Deep functional maps: Structured prediction for dense shape correspondence. In: ICCV, pp 5660–5668
- Liu C, Yuen J, Torralba A (2011) Sift flow: Dense correspondence across scenes and its applications. PAMI 33:978–994
- Liu F, Liu X (2020) Learning implicit functions for topology-varying dense 3d shape correspondence. In: NIPS, Virtual
- Liu Z, Luo P, Wang X, Tang X (2015) Deep learning face attributes in the wild. In: ICCV
- Loper M, Mahmood N, Romero J, Pons-Moll G, Black MJ (2015) Smpl: A skinned multi-person linear model. TOG 34(6):1–16
- Mescheder L, Oechsle M, Niemeyer M, Nowozin S, Geiger A (2019) Occupancy networks: Learning 3d reconstruction in function space. In: CVPR, pp 4460–4470
- Mescheder LM, Geiger A, Nowozin S (2018) Which training methods for gans do actually converge? In: ICML
- Mildenhall B, Srinivasan PP, Tancik M, Barron JT, Ramamoorthi R, Ng R (2020) Nerf: Representing scenes as neural radiance fields for view synthesis. In: ECCV, Springer, pp 405–421
- Mu J, De Mello S, Yu Z, Vasconcelos N, Wang X, Kautz J, Liu S (2022) Coordgan: Self-supervised dense correspondences emerge from gans. In: CVPR
- Niemeyer M, Geiger A (2021) Giraffe: Representing scenes as compositional generative neural feature fields. In: CVPR
- Noguchi A, Sun X, Lin S, Harada T (2021) Neural articulated radiance field. In: ICCV
- Or-El R, Luo X, Shan M, Shechtman E, Park JJ, Kemelmacher-Shlizerman I (2021) StyleSDF: High-Resolution 3D-Consistent Image and Geometry Generation. In: CVPR
- Pan X, Dai B, Liu Z, Loy CC, Luo P (2021) Do 2d gans know 3d shape? unsupervised 3d shape reconstruction from 2d image gans. In: ICLR
- Park JJ, Florence P, Straub J, Newcombe R, Lovegrove S (2019) DeepSDF: Learning continuous signed distance functions for shape representation. In: CVPR, IEEE, pp 165–174, DOI 10.1109/CVPR.2019.00025, URL <https://ieeexplore.ieee.org/document/8954065/>
- Park K, Sinha U, Barron JT, Bouaziz S, Goldman DB, Seitz SM, Martin-Brualla R (2021a) Nerfies: Deformable neural radiance fields. In: ICCV
- Park K, Sinha U, Barron JT, Bouaziz S, Goldman DB, Seitz SM, Martin-Brualla R (2021b) Nerfies: Deformable neural radiance fields. In: ICCV
- Park K, Sinha U, Hedman P, Barron JT, Bouaziz S, Goldman DB, Martin-Brualla R, Seitz SM (2021c) Hypernerf: A higher-dimensional representation for topologically varying neural radiance fields. TOG 40(6)
- Park T, Zhu JY, Wang O, Lu J, Shechtman E, Efros AA, Zhang R (2020) Swapping autoencoder for deep image manipulation. In: NIPS
- Peebles W, Zhu JY, Zhang R, Torralba A, Efros A, Shechtman E (2022) Gan-supervised dense visual alignment. In: CVPR
- Perez E, Strub F, De Vries H, Dumoulin V, Courville A (2018) Film: Visual reasoning with a general conditioning layer. In: AAAI, vol 32
- Pumarola A, Corona E, Pons-Moll G, Moreno-Noguer F (2020) D-NeRF: Neural Radiance Fields for Dynamic Scenes. In: CVPR
- Qi C, Su H, Mo K, Guibas L (2017) Pointnet: Deep learning on point sets for 3d classification and segmentation. In: CVPR, pp 77–85
- Richardson E, Alaluf Y, Patashnik O, Nitzan Y, Azar Y, Shapiro S, Cohen-Or D (2021) Encoding in style: a stylegan encoder for image-to-image translation. In: CVPR
- Sahillioglu Y (2019) Recent advances in shape correspondence. The Visual Computer 36:1705 – 1721
- Schwarz K, Liao Y, Niemeyer M, Geiger A (2020) Graf: Generative radiance fields for 3d-aware image synthesis. In: NIPS
- Shen Y, Yang C, Tang X, Zhou B (2020) Interfacegan: Interpreting the disentangled face representation learned by gans. PAMI PP
- Simonyan K, Zisserman A (2015) Very deep convolutional networks for large-scale image recognition. In: CoRR, vol abs/1409.1556
- Sitzmann V, Martel JN, Bergman AW, Lindell DB, Wetzstein G (2020) Implicit neural representations with periodic activation functions. In: NIPS
- Tancik M, Srinivasan PP, Mildenhall B, Fridovich-Keil S, Raghavan N, Singhal U, Ramamoorthi R, Barron JT, Ng R (2020) Fourier features let networks learn high frequency functions in low dimensional domains. In: NIPS
- Tewari A, Fried O, Thies J, Sitzmann V, Lombardi S, Sunkavalli K, Martin-Brualla R, Simon T, Saragih J,

- Nießner M, Pandey R, Fanello S, Wetzstein G, Zhu JY, Theobalt C, Agrawala M, Shechtman E, Goldman DB, Zollhöfer M (2020) State of the Art on Neural Rendering. *Computer Graphics Forum*
- Tov O, Alaluf Y, Nitzan Y, Patashnik O, Cohen-Or D (2021) Designing an encoder for stylegan image manipulation. *arXiv*
- Tritrong N, Rewatbowornwong P, Suwajanakorn S (2021) Repurposing gans for one-shot semantic part segmentation. In: *CVPR*
- Truong P, Danelljan M, Gool LV, Timofte R (2020a) GOCor: Bringing globally optimized correspondence volumes into your neural network. In: *NIPS*
- Truong P, Danelljan M, Timofte R (2020b) Glu-net: Global-local universal network for dense flow and correspondences. In: *CVPR*, pp 6257–6267
- Truong P, Danelljan M, Gool LV, Timofte R (2021) Learning accurate dense correspondences and when to trust them. In: *CVPR*, pp 5710–5720
- Wang X, Bo L, Fuxin L (2019a) Adaptive wing loss for robust face alignment via heatmap regression. In: *ICCV*
- Wang Y, Sun Y, Liu Z, Sarma SE, Bronstein M, Solomon J (2019b) Dynamic graph cnn for learning on point clouds. *TOG* 38:1 – 12
- Wang Z, Bagautdinov T, Lombardi S, Simon T, Saragih J, Hodgins J, Zollhofer M (2021) Learning compositional radiance fields of dynamic human heads. In: *CVPR*, pp 5704–5713
- Xu J, Wang X (2021) Rethinking self-supervised correspondence learning: A video frame-level similarity perspective. *arXiv*
- Yang G, Belongie S, Hariharan B, Koltun V (2021) Geometry processing with neural fields. In: *Thirty-Fifth Conference on Neural Information Processing Systems*
- Yang S, Jiang L, Liu Z, , Loy CC (2022) Unsupervised image-to-image translation with generative prior. In: *CVPR*
- Yu A, Ye V, Tancik M, Kanazawa A (2021) pixelnerf: Neural radiance fields from one or few images. In: *CVPR*, pp 4578–4587
- Zhang K, Zhang Z, Li Z, Qiao Y (2016) Joint face detection and alignment using multitask cascaded convolutional networks. *IEEE Signal Processing Letters* 23:1499–1503
- Zhang K, Riegler G, Snavely N, Koltun V (2020) Nerf++: Analyzing and improving neural radiance fields. *arXiv*
- Zhang R, Isola P, Efros AA, Shechtman E, Wang O (2018) The unreasonable effectiveness of deep features as a perceptual metric. In: *CVPR*
- Zhang W, Sun J, Tang X (2008) Cat head detection - how to effectively exploit shape and texture features. In: *ECCV*
- Zhang Y, Chen W, Ling H, Gao J, Zhang Y, Torralba A, Fidler S (2021a) Image gans meet differentiable rendering for inverse graphics and interpretable 3d neural rendering. In: *ICLR*
- Zhang Y, Ling H, Gao J, Yin K, Lafleche JF, Barriuso A, Torralba A, Fidler S (2021b) Datasetgan: Efficient labeled data factory with minimal human effort. In: *CVPR*
- Zheng Y, Abrevaya VF, Bühler MC, Chen X, Black MJ, Hilliges O (2022) IM Avatar: Implicit morphable head avatars from videos. In: *CVPR*
- Zheng Z, Yu T, Dai Q, Liu Y (2021) Deep implicit templates for 3d shape representation. In: *CVPR*, pp 1429–1439
- Zhou P, Xie L, Ni B, Tian Q (2021) CIPS-3D: A 3D-Aware Generator of GANs Based on Conditionally-Independent Pixel Synthesis. *arXiv* [2110.09788](https://arxiv.org/abs/2110.09788)
- Zhou T, Krähenbühl P, Aubry M, Huang Q, Efros AA (2016) Learning dense correspondence via 3d-guided cycle consistency. In: *CVPR*, pp 117–126